ELEMENTA
Science of the Anthropocene

Raphael, IA, et al. 2024. Sea ice mass balance during the MOSAiC drift experiment: Results from manual ice and snow thickness gauges. *Elem Sci Anth*, 12: 1. DOI: https://doi.org/10.1525/elementa.2023.00040

RESEARCH ARTICLE

Sea ice mass balance during the MOSAiC drift experiment: Results from manual ice and snow thickness gauges

Ian A. Raphael[1,*], Donald K. Perovich[1], Christopher M. Polashenski[1,2], David Clemens-Sewall[1], Polona Itkin[3], Ruibo Lei[4], Marcel Nicolaus[5], Julia Regnery[5], Madison M. Smith[6], Melinda Webster[7], and Matthias Jaggi[8]

Precise measurements of Arctic sea ice mass balance are necessary to understand the rapidly changing sea ice cover and its representation in climate models. During the Multidisciplinary drifting Observatory for the Study of Arctic Climate (MOSAiC) expedition, we made repeat point measurements of snow and ice thickness on primarily level first- and second-year ice (FYI, SYI) using ablation stakes and ice thickness gauges. This technique enabled us to distinguish surface and bottom (basal) melt and characterize the importance of oceanic versus atmospheric forcing. We also evaluated the time series of ice growth and melt in the context of other MOSAiC observations and historical mass balance observations from the Surface Heat Budget of the Arctic (SHEBA) campaign and the North Pole Environmental Observatory (NPEO). Despite similar freezing degree days, average ice growth at MOSAiC was greater on FYI (1.67 m) and SYI (1.23 m) than at SHEBA (1.45 m, 0.53 m), due in part to initially thinner ice and snow conditions on MOSAiC. Our estimates of effective snow thermal conductivity, which agree with SHEBA results and other MOSAiC observations, are unlikely to explain the difference. On MOSAiC, FYI grew more and faster than SYI, demonstrating a feedback loop that acts to increase ice production after multi-year ice loss. Surface melt on MOSAiC (mean of 0.50 m) was greater than at NPEO (0.18 m), with considerable spatial variability that correlated with surface albedo variability. Basal melt was relatively small (mean of 0.12 m), and higher than NPEO observations (0.07 m). Finally, we present observations showing that false bottoms reduced basal melt rates in some FYI cases, in agreement with other observations at MOSAiC. These detailed mass balance observations will allow further investigation into connections between the carefully observed surface energy budget, ocean heat fluxes, sea ice, and ecosystem at MOSAiC and during other campaigns.

Keywords: Sea ice mass balance, MOSAiC, Arctic sea ice, Transpolar Drift, False bottoms, Snow on sea ice

[1] Thayer School of Engineering, Dartmouth College, Hanover, NH, USA
[2] Cold Regions Research and Engineering Laboratory, U.S. Army Corps of Engineers, Hanover, NH, USA
[3] Department of Physics and Technology, UiT The Arctic University of Norway, Tromsø, Norway
[4] Key Laboratory for Polar Science of the MNR, Polar Research Institute of China, Shanghai, China
[5] Alfred-Wegener-Institut Helmholtz-Zentrum für Polar- und Meeresforschung, Bremerhaven, Germany
[6] Woods Hole Oceanographic Institution, Woods Hole, MA, USA
[7] Polar Science Center, Applied Physics Laboratory, University of Washington, Seattle, WA, USA
[8] WSL Institute for Snow and Avalanche Research SLF, Davos, Switzerland

* Corresponding author:
Email: ian.a.raphael.th@dartmouth.edu

1. Introduction

Arctic sea ice continues to undergo rapid change, with dramatic declines in extent, thickness, and age over the last few decades (Maslanik et al., 2007; Meier et al., 2007; Kwok, 2018; Meier et al., 2021). First-year ice (FYI) is now the dominant ice type in the Arctic, and the remaining second-year ice (SYI) and multi-year ice (MYI) is significantly younger and thinner. The factors contributing to this loss are likely changing as the ice pack becomes thinner, younger, and less extensive. We need an up-to-date understanding of Arctic sea ice mass balance in order to ensure its accurate representation in climate models, including an understanding of the energy fluxes influencing ice growth and melt.

Positioned at the boundary of the ocean and atmosphere, sea ice occupies the key interface in the Arctic system, governing the flow of heat, light, and mass

between the ocean and the atmosphere. In addition to *governing* mass and energy transfer, sea ice is also *impacted* by fluxes from the atmosphere and ocean, responding through growth and ablation. Monitoring ice growth, surface melt, and bottom melt over time provides an integrated measure of atmospheric and oceanic heat fluxes. This approach helps us build a process-based understanding of ice mass balance that is generalizable and suitable for climate modeling.

Mass balance observations have been conducted at many prior sea ice field experiments (Koerner, 1973; Perovich et al., 2003; Perovich and Richter-Menge, 2006) and are collected on an ongoing basis by autonomous ice mass balance buoys (Richter-Menge et al., 2006; Perovich et al., 2014; Lei et al., 2018). In situ measurement using hotwire thickness gauges and ablation stakes is one of the simplest, most robust methods of observing local sea ice mass balance. These instruments have also been deployed on prior field experiments (Untersteiner, 1961; Perovich et al., 2003; Roesel et al., 2018). On the Multidisciplinary Drifting Observatory for the Study of Arctic Climate (MOSAiC) campaign, we had the rare opportunity to deploy large numbers of hotwire thickness gauges and ablation stakes across an ice floe so that we could observe and understand ice mass balance and its variability at the floe scale. The campaign also provided an opportunity to measure the ice mass balance in the context of detailed observations of surface and ocean heat fluxes.

A similar program of paired mass balance and heat flux observations was carried out during the Surface Heat Budget of the Arctic (SHEBA) field experiment in 1997–1998 (Uttal et al., 2002). However, pack-ice conditions have changed substantially since then. Describing the general behavior of perennially thinning FYI and SYI and the differences between the two ice types is a key part of understanding the changing Arctic ice cover. The MOSAiC floe was chosen to represent this "new" Arctic, as it was composed of FYI and SYI with very thin initial conditions (Krumpen et al., 2020).

In this article, we report on the ice mass balance observations made using hotwire thickness gauges and ablation stakes during MOSAiC, compare the results to prior campaigns, and connect ice thickness changes to specific processes. Using the Icepack single column model (Hunke et al., 2023), we demonstrate that thinner snow and ice conditions contributed to high growth compared to historical observations. We also make estimates of the effective thermal conductivity of snow on sea ice, and consider the effects on ice mass balance of under-ice meltwater and false bottoms during the melt season.

In addition to hotwire thickness gauges and ablation stakes, several other methods for measuring snow and ice mass balance were implemented on MOSAiC, including repeat ground-based surveys using an electromagnetic (EM) induction device (Itkin et al., 2023); repeat aerial EM surveys (Belter et al., 2021); and various types of autonomous ice mass balance buoys (IMBs) (Koo et al., 2021; Lei et al., 2022; Perovich et al., 2023). Of these studies, Lei et al. (2022) offer the most relevant comparison, presenting an analysis of ice thickness point measurements which resolve surface and basal change. Ultimately, we draw the common conclusion that initial ice thickness is a primary determining factor for ice winter growth. We find similar timings for growth and melt transitions. While Lei et al. (2022) provide valuable temperature measurements in the ice and higher temporal resolution, our dataset offers higher measurement precision (0.01 m vs. 0.04 m) and a greater number of sampling locations (137 vs. 23). Although a thorough comparison of the numerous and highly complementary mass balance measurements made on MOSAiC is still needed, this study is intended to provide an analysis of the hotwire thickness gauge and ablation stakes measurements and to place them in context with similar historical observations.

Smith et al. (2022) and Salganik et al. (2023a) both present observations of false bottoms and under-ice meltwater layers collected on MOSAiC. These studies are valuable for their relatively extensive areal observations of the features. Salganik et al. (2023a) also provide a review of the existing literature and underlying physical processes influencing meltwater layers and false bottoms and an estimation of their influence on ice mass balance. Further, Smith et al. (2023) conducted a thorough synthesis of recent work on false bottoms and under-ice meltwater layers, with a focus on MOSAiC observations. They explored the impacts of these features across the sea ice system, with attention to ocean, ice, gas-flux, and ecology processes. Both Smith et al. (2023) and Salganik et al. (2023a) observed that false bottoms lead to an approximate 8% reduction in basal melt. We found a greater effect on mass balance from false bottoms, estimating a nearly 50% reduction in basal melt over the course of our observations. Further comparison is needed to determine the cause of the difference. Our paired false bottom and mass balance observations complement these various studies by offering a relatively long time series, high measurement precision, and a higher number of individual sampling points.

2. Methods

2.1. MOSAiC concept and measurement program

The MOSAiC expedition was a year-long Arctic drift experiment carried out in the central Arctic Ocean from October 4, 2019, to September 20, 2020, aboard the German research icebreaker FS *Polarstern* (**Figure 1**). Detailed descriptions of the expedition are available in several overview papers (Nicolaus et al., 2022; Rabe et al., 2022; Shupe et al., 2022). Sea ice studies were an integral component of MOSAiC. The MOSAiC plan proposed occupying a single ice floe throughout an annual cycle. Due to rapid drift and logistical constraints, however, the expedition was carried out at three distinct scientific camps on two different ice floes. The first floe was occupied during two intervals from October 4, 2019, to July 31, 2020 (MOSAiC Legs 1–4), with autonomous observations from May 16, 2020, to June 19, 2020, during an off-site personnel rotation (Nicolaus et al., 2022). The first floe was abandoned on July 31, 2020, once it had reached Fram Strait, where it quickly disintegrated.

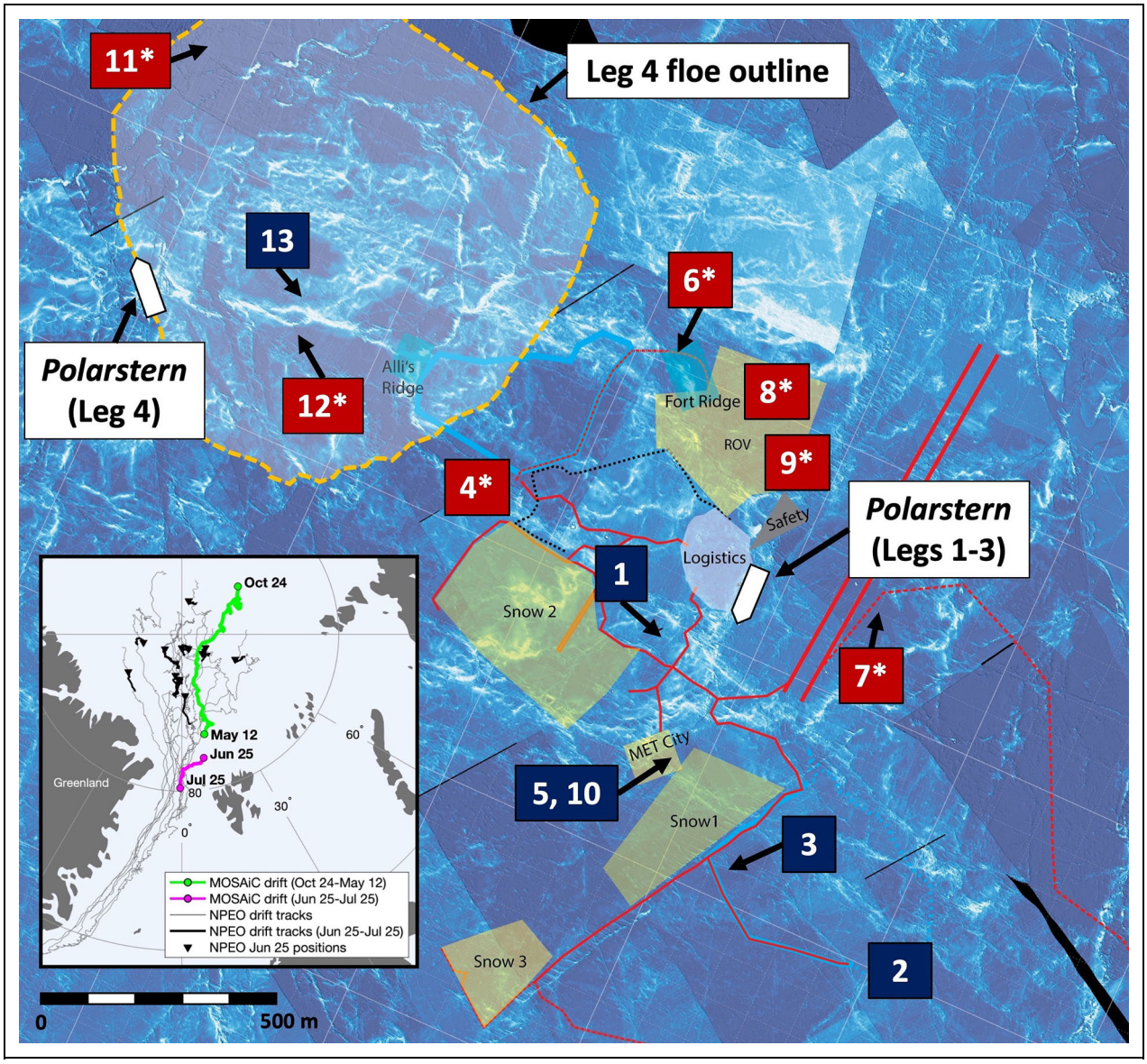

Figure 1. Map of stakes sites on MOSAiC from October 4, 2019, to July 31, 2020. Site numbers correspond to the following sites during Polarstern Legs 1–4: Bow Stakes (1), Stakes 2 (2), Stakes 3 (3), Stakes 1 (4*), MET Stakes (5), Ridge Ranch (6*), Runaway Stakes (7*), Miss Stakes (8*), Steak Stakes (9*), Return of the MET Stakes (10), Drone Bones (11*), Reunion Stakes (12*), and Beanpole Stakes (13). Asterisks indicate first-year ice sites (red site labels). Second-year ice sites are labeled in dark blue. The locations of FS Polarstern on Legs 1–3 (October 4, 2019, to May 16, 2020) and on Leg 4 (June 19, 2020, to July 31, 2020) are indicated. The locations of several snow (Snow 1–3), ice (Fort Ridge, ROV), and atmosphere (MET City) sampling sites are also indicated. Primary ice camp roads are shown as red lines. The Leg 4 floe is outlined with a dashed yellow line. The basemap is a topographic relief map generated from a composite aerial LiDAR scan from March 5, 2020; the vertical range spans approximately 2 m, with lighter shades indicating higher features. The inset map shows the MOSAiC drift path during the growth period (green) and melt period (pink), as well as the full drift tracks (gray) of the NPEO buoys analyzed in this manuscript. The thicker, black traces show the NPEO buoy drift tracks during the MOSAiC melt period (June 25–July 25); the inverted black triangles show the location of each NPEO buoy on June 25.

The expedition then reestablished at a second location near the North Pole on August 21, 2020, to observe fall freeze-up (MOSAiC Leg 5). This camp configuration resulted in a multi-part mass balance observational record. These observations highlight a key reality of the new Arctic: due to anomalously high drift speeds (Rinke et al., 2021), ice that entered the western (upstream) side of the Transpolar Drift (TD) during freeze-up in 2019 fully transited the Arctic and melted in Fram Strait before the start of fall freeze-up in 2020. Thus, this ice did not have the opportunity to undergo a full annual cycle. In this study, we exclude results from the third camp, which were made on a different collection of ice floes in a different geographic location. We focus on observations from the first two camps in order to ensure consistency in the mass-balance time series.

2.2. Ablation stakes and hotwire thickness gauges

Ablation stakes and hotwire thickness gauges (**Figure 2**) are frequently used to obtain point mass balance measurements of snow and sea ice (Untersteiner, 1961; Hanson, 1965; Perovich et al., 2003). They offer several advantages for studying ice mass balance processes. Because they provide a direct and manual measurement of snow and ice interfaces, their results require minimal processing and few assumptions in their interpretation. Second, they are a point measurement: repeat measurements can be used to determine the response of a specific location in the ice to environmental forcings. These measurements complement repeat transect surveys often made with snow depth probes and electromagnetic induction (EM) instruments (Eicken et al., 2001; Roesel et al., 2018, Itkin et al., 2023). EM instruments are well suited for statistical analyses of snow- and ice-thickness distributions in a given area. However, they cannot be used to delineate between surface and bottom changes, and do not precisely identify the ice thickness at a given point due to the footprint of the instrument and errors in co-locating snow depth measurements. Furthermore, the uncertainties of ice thickness retrieval are 0.05–0.10 m over level sea ice and larger over deformed ice (Eicken et al., 2001; Haas et al., 2009). Ablation stakes and hotwire thickness gauges have relatively high measurement precision, with a total thickness uncertainty estimated at about 1 cm, and are installed at a fixed location. They allow us to distinguish between thickness change at the surface versus the bottom of the ice, which is particularly important in determining the influence of atmospheric and oceanic heat fluxes on ice mass balance. Further, because they require manual measurement, detailed contextual information may be recorded, which is usually not available for autonomous measurements made by ice mass balance buoys.

The ablation stakes used on MOSAiC were either 2-m-long wooden stakes painted white to minimize solar heating and melt-out, or 3-m-long white PVC stakes. Both had graduated metric tape affixed along their length. We installed the stakes in 0.05 m diameter holes drilled into the ice using ice augers. We allowed them to freeze into the ice with 1.5 m beneath the ice surface and the remaining length extending up through the snow and into the air. The ablation stakes provided a fixed reference point from which to measure the relative position of the ice or snow surface, which we read directly from the graduated

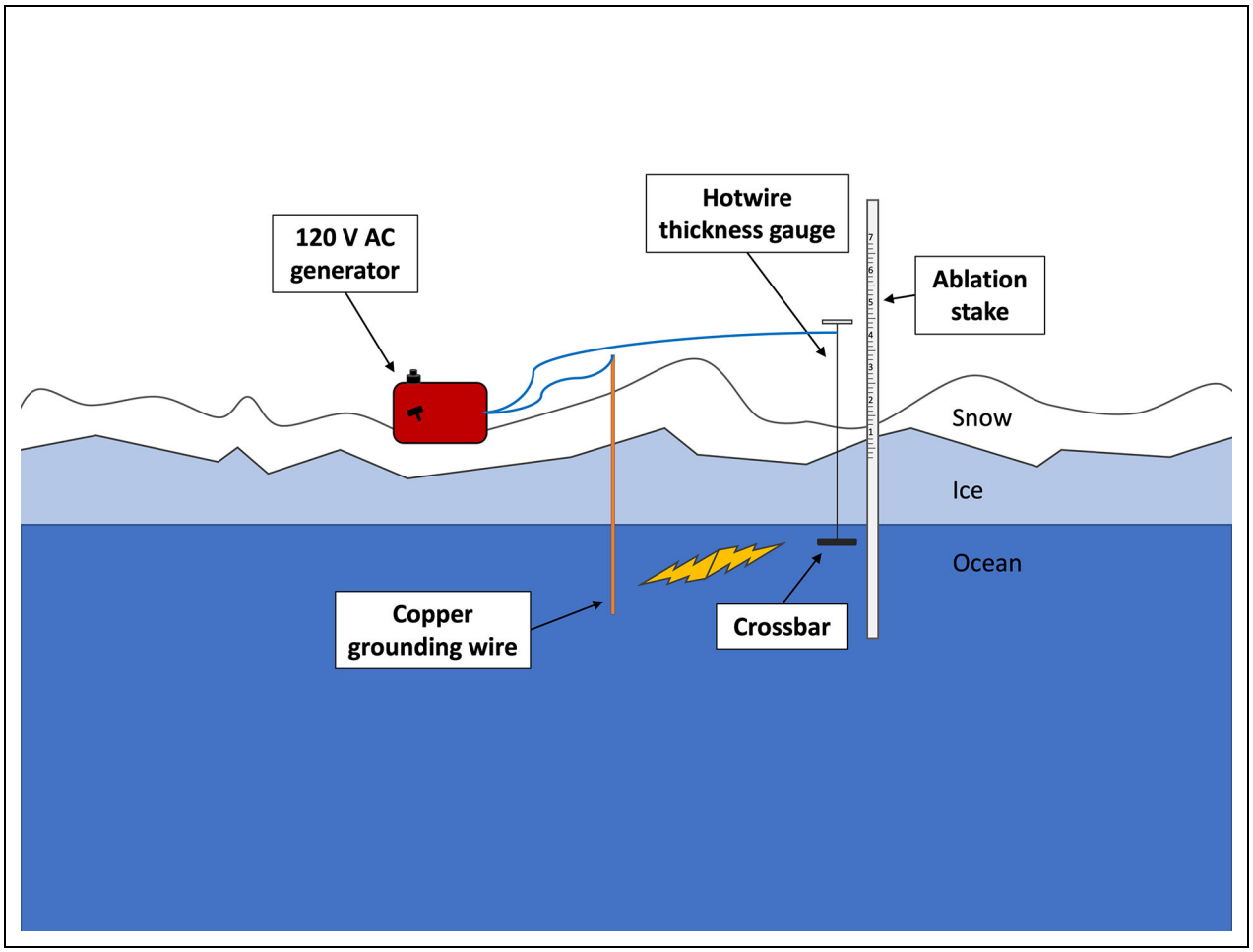

Figure 2. Diagram of an ablation stake and hotwire thickness gauge. Measurement stations consisted of an ablation stake and hotwire thickness gauge. Each stake had a graduated tape affixed along its length. A copper grounding wire was installed at each site. A generator was used to resistively heat the thickness gauge, with seawater completing the circuit. See Untersteiner (1961) for a detailed description of the method.

tape to the nearest 0.005 m. We assumed that the snow–ice interface did not change until snow melt was complete. We did not observe flooding, snow-ice formation, or other types of surface ice formation at any of the stakes during the growth season.

Hotwire thickness gauges consisted of an approximate 4 m length of 2.5 mm diameter stainless steel wire, with a 0.10 m long, 0.025 m diameter steel crossbar affixed to one end and a wooden handle affixed to the other. We installed them in 0.05 m diameter holes drilled directly next to each stake, so that the crossbar hung in the ocean below the ice, while the wooden handle remained above the surface. We made measurements of the ice bottom position by running electrical current through the gauge until it melted free of the ice, then pulling up on the gauge until the crossbar contacted the bottom of the ice (Untersteiner, 1961). We then measured the position of the handle against the graduated tape on the ablation stake.

We made measurements of initial ice thickness and snow depth during installation, as well as measurements of initial ice and snow surface and ice bottom positions. Changes in the positions of each interface (ice bottom, ice surface, snow surface) over subsequent measurements directly corresponded to changes in ice and snow thickness. We used the measurements of initial snow depth and ice thickness made during installation to convert interface position measurements to absolute ice thickness and snow depth. Throughout the manuscript, we refer to an ablation stake/hotwire thickness gauge pair simply as a "stake."

We deployed iButton DS1925 combined temperature sensor/datalogger units at the snow–ice interface at eight FYI stakes (Section 3.4; Raphael et al., 2024). These sensors recorded hourly temperature readings with 0.5°C accuracy and 0.0625°C precision. We used these data in snow thermal conductivity calculations (Section 4.2).

2.3. Observing false bottoms

A false bottom is a secondary layer of ice that forms beneath the sea ice at the interface between the upper ocean mixed layer and an overlying, relatively fresh, meltwater layer (Notz et al., 2003; Smith et al., 2022). The meltwater originates from percolated surface snow and ice melt, as well as bottom melt. Because of the buoyancy of this relatively fresh and warm meltwater, it can accumulate in inverted basins beneath the ice, remaining strongly stratified from the mixed layer. As heat diffuses from the meltwater into the mixed layer, a layer of ice—a "false bottom"—can form between the two strata (Notz et al., 2003). We observed false bottoms at several stakes during the melt season. Smith et al. (2022) observed and measured false bottoms in the vicinity of the site using independent methodology. We continued to note the presence or absence of false bottoms at the site "by feel," that is, noting when the crossbar contacted a solid that could not reasonably be the true ice bottom. In some cases, we were able to maneuver the crossbar through preexisting holes in the false bottom, which likely existed due to enhanced melt of the false bottom around the hotwire and crossbar. In these cases, we measured false bottom thickness as the gauge difference between the crossbar resting above, then below the false bottom (accounting for the thickness of the crossbar). We also measured the distance between the false bottom and the "true" bottom of the ice. These measurements had the same precision as standard stakes measurements; however, due to the presumed enhanced melt around the hotwire, our estimates of false bottom thickness are likely low-biased.

Our observations of bottom melt (which we use interchangeably with "basal melt") represent the "true" bottom of the ice. When reaching the true ice bottom with the crossbar was not possible, bottom measurements were not made and thus do not appear in the dataset. This occurred regularly for only 3 stakes during the melt season.

2.4. Measurement sites

We measured ice mass balance at 137 individual stakes over the growth and melt seasons on MOSAiC. Individual stakes were clustered together at 13 different sites to capture the small- and large-scale spatial variability of the ice mass balance (**Figure 1**). We installed the stakes at each site using regular-grid or transect patterns with spacings of 5–10 m between stakes, depending on the site. This distribution produced a random sampling within each site. Individual site maps are available in the stakes data archive (Raphael et al., 2022), and detailed maps showing the location of sites in relation to other MOSAiC installations are available in Nicolaus et al. (2022). The distribution of stakes within each site captured the mean behavior and variability of ice mass balance given a certain ice type and/or local conditions. Variability between individual stakes within a site represents small-scale spatial variability of ice mass balance processes given common ice type and conditions. Variability between sites gives insight into how ice mass balance processes differ between ice types and conditions. Hereafter, population standard deviations are given as a plus/minus range after mean or median values, for example, mean $\pm$ standard deviation.

Sites were chosen to represent the range of ice types and conditions at MOSAiC, as well as to co-locate stakes measurements with atmospheric and oceanic measurements and other ice and snow mass balance measurements. Seven sites were installed on FYI (including two lead ice sites formed in midwinter), and six on SYI. We installed the sites at various times throughout the expedition, as some sites were destroyed or became inaccessible due to ice dynamics (**Figure 3**). We measured each site approximately every 2 weeks (corresponding to about 0.15 m of ice growth) during the growth season and every 1–3 days (0.02–0.06 m of combined melt) during the melt season.

2.5. Icepack sea ice column modeling

To explore factors contributing to differences in ice growth between MOSAiC and SHEBA, we used Icepack (Hunke et al., 2023), the column physics submodule of the CICE sea ice model (Hunke et al., 2017). Icepack simulates thermodynamic growth and melt, and dynamic changes to the ice thickness distribution and ice state (e.g., salinity, enthalpy, etc.) for a domain with fixed areal

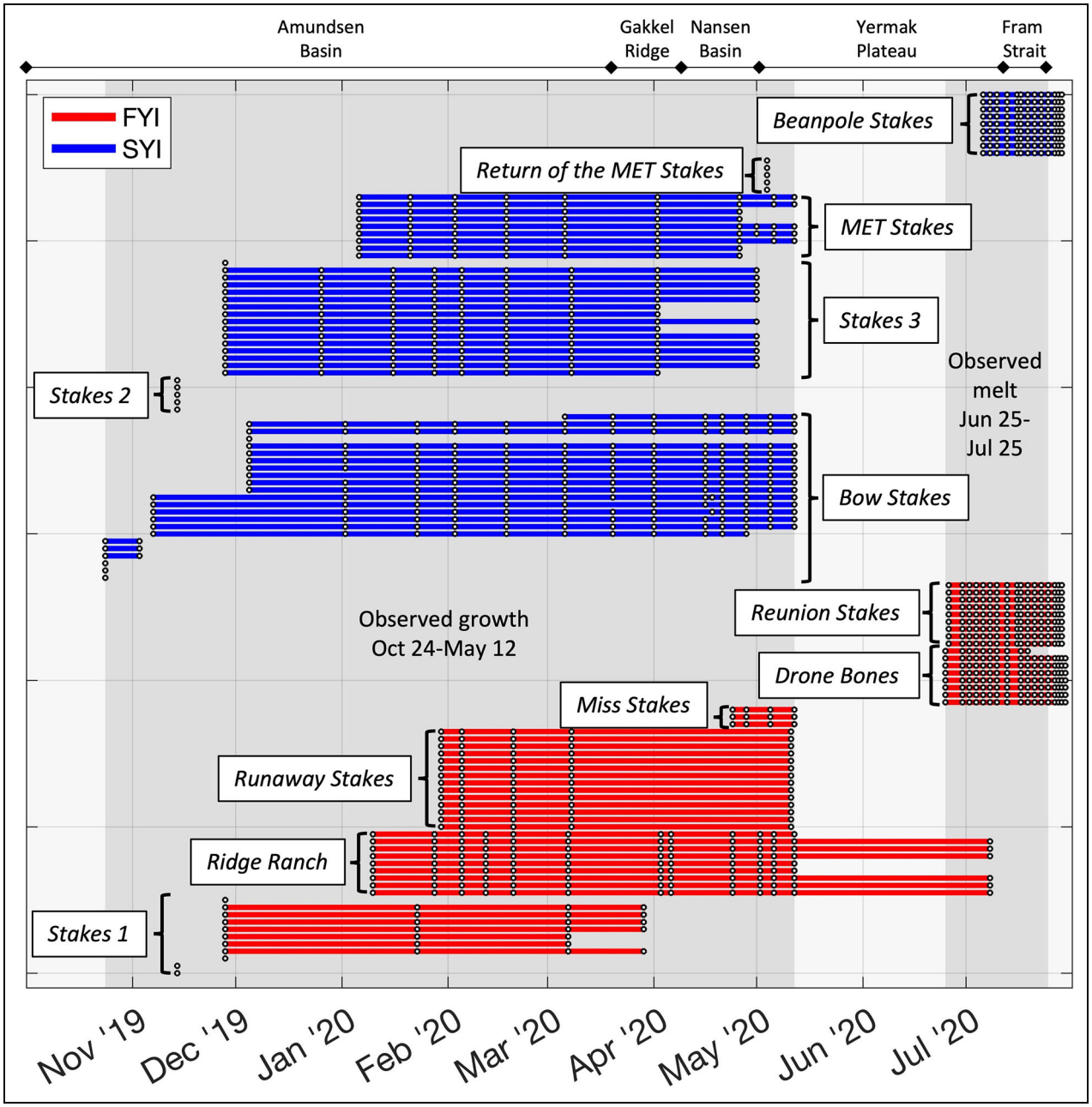

Figure 3. Operational and sampling dates of MOSAiC stakes. The operational periods for individual stakes on Legs 1–4 are shown as blue or red solid horizontal bars. Red indicates first-year ice; blue, second-year ice. Stakes are grouped and labeled by site. White dots mark measurement dates for each stake. We made measurements every 2–3 weeks during the growth season, when change was relatively slow, and every 1–3 days during the melt season, when change was more rapid. The gray-shaded areas indicate the growth and melt periods presented in this study. The labels above the figure indicate the regional location of the ice camp throughout the drift.

extent. CICE uses Icepack within each Eulerian grid cell (i.e., domain with fixed extent and location) of the CICE grid. We used Icepack to simulate drifting Lagrangian parcels of ice corresponding to the manual mass balance sites at MOSAiC and SHEBA.

Icepack uses an ice thickness distribution (ITD; Bitz et al., 2001) to represent the ice cover. The ITD represents the ice cover as a set of ice thickness categories (typically 5), each of which is defined by non-overlapping category limits (e.g., the thickness limits for category two may be 0.6–1.4 m). Each thickness category comprises an evolving ice thickness and fractional ice area. At each time step, thermodynamic changes are simulated independently for each category using mushy layer physics (Turner and Hunke, 2015), assuming the ice and snow within the category is horizontally uniform. Shortwave radiative transport is simulated with a Delta-Eddington parameterization (Briegleb and Light, 2007). After ice growth/melt has been computed for each category, a linear remapping scheme transports ice volume and area between categories to respect category limits while conserving mass (Lipscomb, 2001). As we are focused on wintertime growth at non-

deforming mass balance sites, the melt pond and mechanical redistribution parameterizations are not relevant for this work.

For standalone Icepack simulations (i.e., not coupled to an atmosphere model), the required atmospheric forcings are time-resolved precipitation, air temperature, specific humidity, wind speed, and downwelling longwave and shortwave radiation. With the exception of precipitation, we derived these quantities primarily from the MOSAiC MET City atmospheric measurements (Cox et al., 2023a). We filled gaps in the MET City record with measurements from the Automated Surface Flux Stations (Cox et al., 2023b; 2023c; 2023d). See Clemens-Sewall et al. (2024) for details of gap-filling. These data have a native 1-minute resolution, so we averaged them to the model's 1-hour time step. Precipitation forcing was interpolated from the snow accumulation measurements at the mass balance sites of each campaign (MOSAiC, SHEBA), such that the simulated accumulation matched the observations. Finally, in standalone Icepack simulations, we have a simple, well-mixed slab ocean mixed layer with prognostic temperature and prescribed salinity, mixed layer depth, and oceanic heat flux convergence (which we assume can be approximated by the turbulent heat flux over the halocline). The prescribed forcings were derived from daily Ocean City measurements (Schulz et al., 2023) and linearly interpolated to the model's hourly time step.

3. Results

3.1. Installation measurements and general observations

Here we present the time series of thickness data from 121 stakes, many of which were not recorded for the entire time frame. We excluded 10 stakes installed at the third camp, and 6 that were removed in the quality control process. The ice experienced significant deformation throughout the growth and melt seasons (Krumpen et al., 2021). Of the 94 stakes deployed during the growth season at the first scientific camp, only 8 survived until the second scientific camp was established during the melt season. These 8 stakes were only measured once during the melt season as ice dynamics made them difficult to access. The additional 27 stakes installed during the melt season (*Reunion Stakes, Drone Bones,* and *Beanpole Stakes*) were lost when the floe melted in Fram Strait.

Initial thicknesses for undeformed SYI ranged from 0.56 m to 0.78 m at the time of installation (late October), with a median thickness of 0.66 m. Deformed SYI stakes had a median initial thickness of 1.60 m and a maximum of 2.16 m. The seasonal cycle of winter ice growth and summer melt is apparent in **Figure 4a**, with thickness increasing steadily over approximately 9 months of growth and melting rapidly during the melt season. Some ice growth had already occurred between SYI bottom growth onset (as early as October 14, 2019; Lei et al., 2022) and the first installation of SYI stakes. Independent

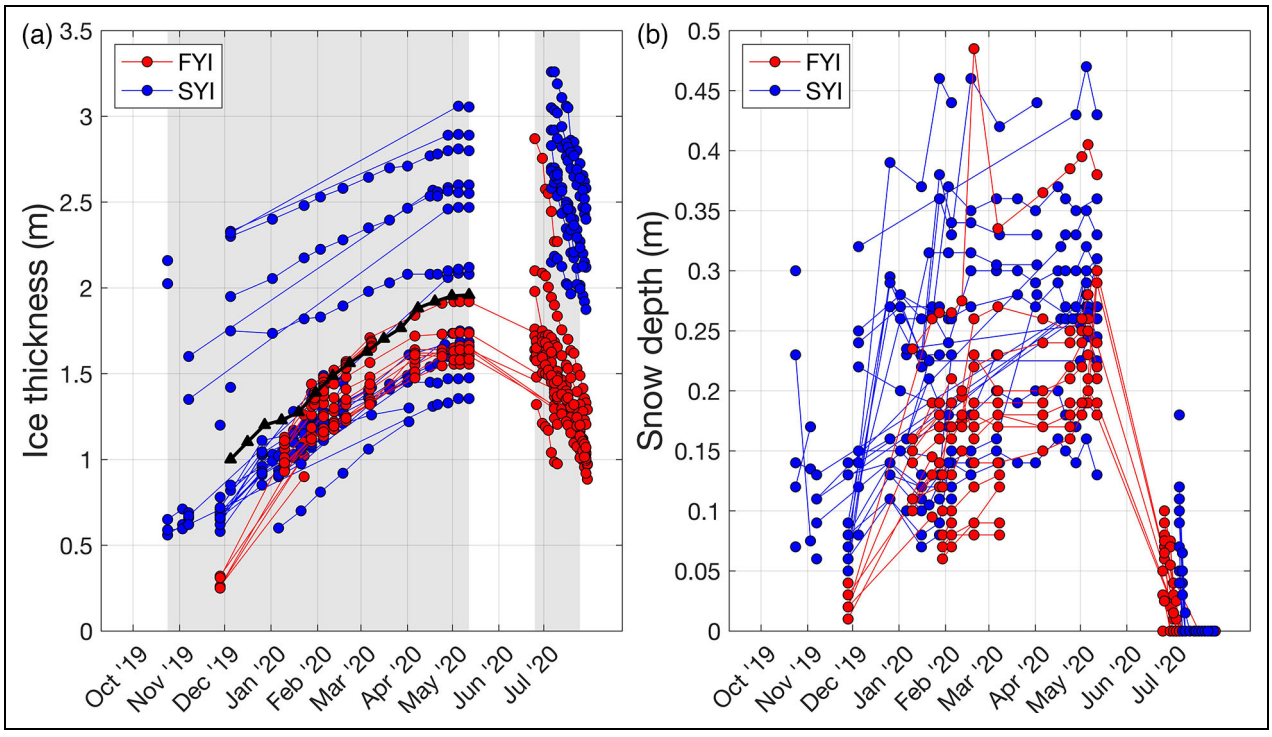

Figure 4. Time series of snow and ice thickness measurements. Panel (a) shows measured ice thickness for individual stakes on Legs 1–4 (October 4, 2019, to July 31, 2020). Panel (b) shows snow depth at individual stakes over the same period. First-year ice (FYI) stakes are shown in red, second-year ice (SYI) stakes, in blue. Filled circles indicate measurement dates. Traces are interpolated linearly between measured values. The black trace with triangular markers in panel (a) shows the average ice thickness at regular query points, determined by averaging the value of all linearly interpolated ice thickness traces at the time of each query point. The grey-shaded areas indicate the growth and melt periods presented in this study.

observations from four SIMB3 ice mass balance buoys (Planck et al., 2019) deployed at other floes in the region in similar SYI (Perovich et al., 2023) indicated that an average growth of approximately 0.23 m had occurred between growth onset and November 15. The thin, undeformed condition of the sampled SYI indicated that the ice had only narrowly survived the summer melt season. During initial MOSAiC floe exploration and setup, we also observed that the ice was porous and rotten.

Over the course of the growth season, two FYI sites (*Stakes 1* and *Miss Stakes*) were specifically installed on newly refrozen leads formed later in the growth season. *Stakes 1* was installed on November 28, 2019, in a refrozen lead that opened around November 16, intended to capture the growth of thin, new ice. Excluding one outlying (likely rafted) stake, the site had an average initial thickness of 0.28 ± 0.03 m and a minimum initial thickness of 0.25 m. We removed *Miss Stakes* from the dataset during the quality control process; they are not considered in this analysis.

We installed the remainder of the FYI sites beginning in January, several months after initial ice formation had begun in late September. At that time, the average installation thickness for FYI that had formed at the beginning of the growth season was 1.00 ± 0.39 m.

Seasonal transition timing from winter growth to spring melt was similar for all ice types (**Figure 4a**). Growth ended between April 28 and May 12, 2020, depending on the site. The thicknesses of FYI, late-forming first year (lead) ice, and undeformed SYI all ultimately peaked in a similar range. FYI reached a median maximum thickness of 1.64 ± 0.11 m. SYI reached a median maximum thickness of 1.66 ± 0.23 m. No undeformed SYI grew thicker than 2.09 m, and level FYI had a similar maximum recorded thickness of 1.92 m. Only thermodynamic growth was noted; stakes cannot be used to measure dynamic growth, and no snow-ice formation was observed.

Surface melt onset (surface skin temperature above 0°C) occurred during a period when the ice floe was not occupied. Other records from autonomous surface range-finders and surface energy balance observations indicate that surface melt onset occurred on approximately May 25 (Cox et al., 2021), and surface melt ponds were visible in satellite imagery by May 28 (Webster et al., 2022). *Bow Stakes* and *Ridge Ranch* showed brief episodes of bottom melt beginning on April 21 and April 24, respectively, which coincided with intense low-pressure systems bringing high wind and ice drift speeds (Shupe et al., 2022). Approximately half of the stakes at these two sites experienced bottom melt by May 12. Sustained bottom melt began during the logistics gap between May 16 and June 19. The 2020 fall freeze-up was not documented in this record because the ice floe drifted into the North Atlantic and did not survive the summer season.

A mean of 0.08 m of snow accumulation had already occurred prior to the first site installations, which began on October 24, 2019 (**Figure 4b**). Snow depth increased rapidly during the early part of the growth season (October–January) followed by little accumulation through late April. A small increase in snow depth occurred in late April and early May. Maximum snow depth occurred in early May and on SYI averaged 0.30 ± 0.08 m, while maximum snow depth on FYI averaged 0.23 ± 0.08 m. SYI sites tended to gain more snow than FYI during accumulation events. On both ice types, snow depth was highly spatially variable and moderately temporally variable throughout the time series due to snow erosion, transport, redeposition, and increased entrapment in deformed ice areas.

Upon reoccupation of the ice camp in June 2020, significant surface melt had already occurred, and the average snow depth had decreased to 0.02 m on FYI and 0.06 m on SYI. The remaining snow persisted primarily in drifts located adjacent to deformed ice. Snow depth reached 0 cm at all stakes by July 13, 2020. Although there were several light snowfall events during the melt season, measurable accumulation did not occur.

3.2. Growth season

Total ice growth over the growth season (estimated from growth onset) varied substantially by ice age. SYI grew an average of 1.23 m, while FYI grew 1.67 m, an average of 0.44 m more growth than SYI. We determined FYI growth simply as the peak ice thickness of FYI recorded during the winter, as this thickness represents the total growth that had occurred since the beginning of the season. Because we do not have SYI initial thickness measurements coinciding with the onset of growth, total SYI growth was determined by differencing the average thickness of SYI stakes measured between October 24 and November 28 from the average thickness of SYI stakes measured between May 1 and May 6, 2020, then adding the growth prior to November 15 from SIMB3 buoys installed in undeformed SYI. We assume here that the SYI stakes measured during the May period were installed on ice similar to the ice measured during the November period.

We determined time-averaged growth rates between all consecutive observations for each stake, then found the spatial average of all stakes at monthly intervals (**Figure 5a**). We determined growth rates for each stake over each measurement interval as $\frac{H_1 - H_0}{t_1 - t_0}$; that is, the difference in ice thickness measurements ($H_1 - H_0$) divided by the time interval between the two measurements ($t_1 - t_0$). This calculation leads to a total percent uncertainty in average growth rate for each stake of $\frac{\delta h_b}{\Delta h_b} + \frac{\delta t}{\Delta t}$. The terms Δh_b and Δt are the change in bottom position and the change in time, respectively, during each interval; their typical values were on the order of 0.08 m and 10 days, respectively, during the growth season. The term δh_b is the uncertainty in bottom interface change (± 0.01 m), which is twice the interface detection measurement uncertainty (± 0.005 m) to account for uncertainty in measurements at both t_0 and t_1. The term δt is twice the measurement uncertainty in time, estimated at approximately ±4 hours. Typical uncertainties in the rates presented in **Figure 5a** are thus approximately 14%. Values in **Table 1** were calculated over the season, leading to season growth-rate uncertainties on the order of 1%. Further, all values in **Table 1** are presented as mean ±

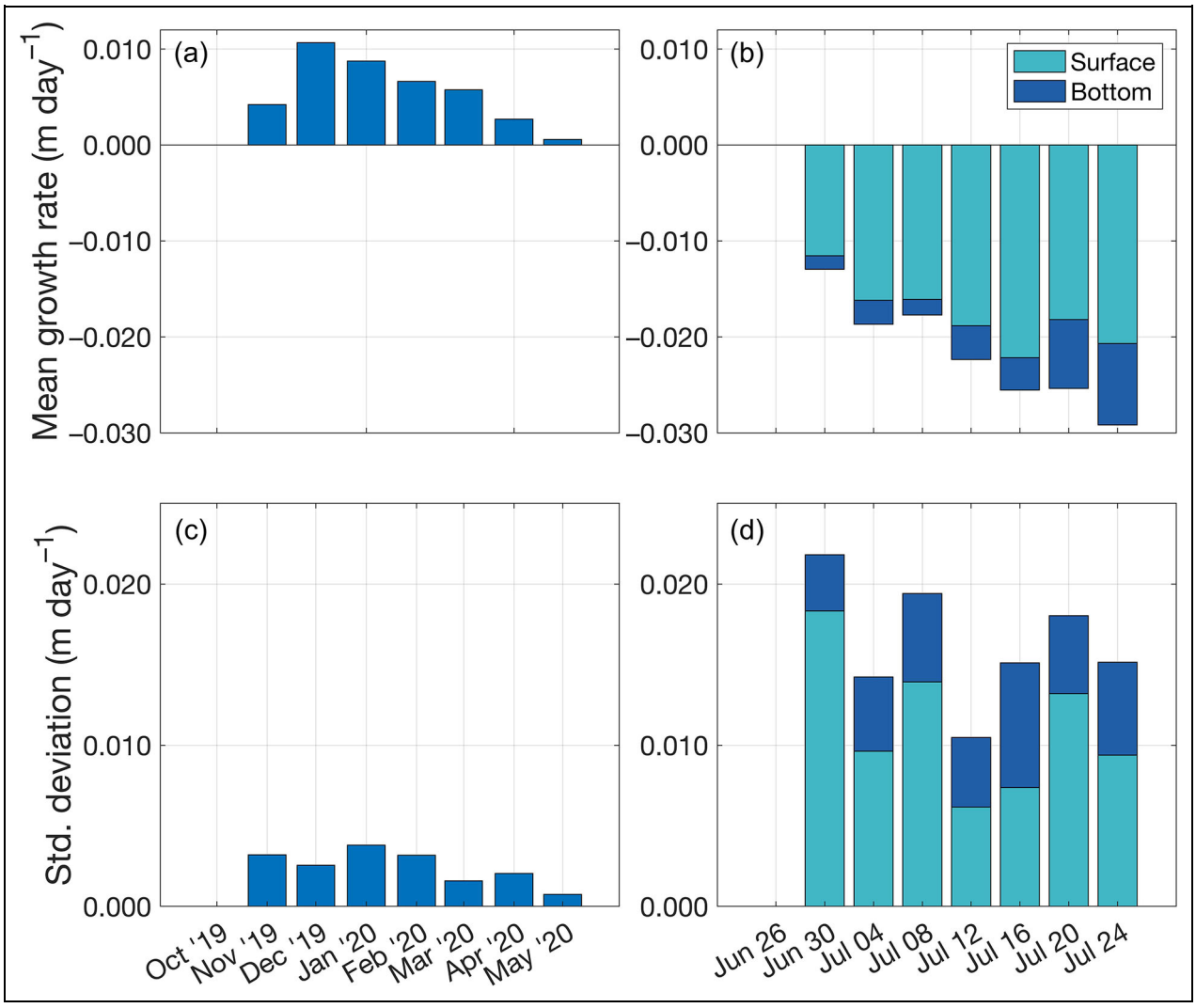

Figure 5. Growth and melt rates and their variabilities. Average growth rates for all stakes are shown here in panels (a) and (b), with monthly averages during the growth season (a), and weekly averages during the melt season in 2020 (b). Their variabilities (population standard deviations) are shown in the panels (c) and (d) with identical time bins. Melt rates and standard deviations are separated into surface melt (teal) and bottom melt (blue). Negative values indicate ice melt.

Table 1. Mean growth and melt rates for first-year ice (FYI) and second-year ice (SYI) stakes

Ice Age	Mean Growth Rate (m day^{-1})[a]	Mean Total Melt Rate (m day^{-1})[b]	Mean Surface Melt Rate (m day^{-1})[b]	Mean Basal Melt Rate (m day^{-1})[b]
FYI	0.008 ± 0.0005	−0.021 ± 0.005	−0.017 ± 0.003	−0.004 ± 0.002
SYI	0.006 ± 0.0004	−0.020 ± 0.007	−0.016 ± 0.005	−0.004 ± 0.002

[a]Calculated for October 4, 2019, to May 12, 2020 (FYI), and October 14, 2019, to May 12, 2020 (SYI).

[b]Calculated for June 25–July 25, 2020.

population standard deviation, a measure of spatial variability rather than uncertainty.

Peak growth rates occurred in December, with an average maximum (combined FYI and SYI) of 0.011 m day^{-1}. Season-long (October 4, 2019, to May 12, 2020) averages indicate that FYI grew faster than SYI (**Table 1**). Measurements at thin-ice sites (*Stakes 1, Miss Stakes*) indicate that FYI initially grew at least twice as fast as SYI, with recorded growth rates of up to 0.02 m day^{-1}. This value is likely still a significant underestimate of initial ice growth rate, as growth rates are expected to decrease inversely with ice thickness (Maykut, 1986) and even the thinnest ice cases had reached 0.25 m before observations began. The observed high growth rates gradually reduced as the ice grew to a thickness comparable to SYI (approximately 1.00–1.50 m in mid-January). The difference in total

growth between FYI and SYI therefore primarily occurred early in the growth season. Spatial variability (population standard deviation) in growth rate generally decreased over the growth season, likely due to the decreasing significance of snow depth and ice thickness variability compared to increasing ice thickness (**Figure 5c**). Growth rates declined monotonically after December, reaching 0 m day^{-1} on May 12. We found no relationship between mean growth rate and standard deviation in growth rate during the growth season.

3.3. Melt season

3.3.1. Melt timing, magnitude, and variability

The overall amount of melt at the floe was quite simple in some ways: all ice entered the North Atlantic through Fram Strait, broke up around July 31, and presumably melted completely thereafter. However, for comparison with prior work, we are primarily interested in the thermodynamic balance prior to encountering near surface Atlantic water on about July 25 (Rabe et al., 2022). We therefore present the total ice melt as the amount of melt occurring between June 25 and July 25. All other melt season results are presented for this same period.

The ice station was not manned during surface melt onset (Nicolaus et al., 2022), which occurred in mid-May (Shupe et al., 2022). Through autonomous observations, we know that surface (snow) melt commenced on May 25 (Cox et al., 2021), though snow remained at all sites when we re-occupied the floe on June 25. Upon reoccupation, we installed three new stake sites on FYI and SYI. The newly installed FYI stakes had a mean thickness of 1.39 $\pm$ 0.13 m, and SYI stakes had a mean thickness of 2.57 $\pm$ 0.32 m. The average snow depth at that time was 0.02 m (June 25) on FYI and 0.06 m on SYI (July 6). Snow melt completion varied by site from June 28 to July 13, with deeper snow near deformed ice persisting longer into this range. Total ice melt at FYI sites averaged 0.63 $\pm$ 0.13 m. Surface ice melt on FYI far exceeded basal melt, with a mean of 0.52 $\pm$ 0.10 m; basal melt contributed 0.11 $\pm$ 0.05 m. SYI sites experienced slightly less total and surface melt, with an average of 0.60 $\pm$ 0.17 m total melt and 0.47 $\pm$ 0.15 m surface melt. We observed slightly more basal melt on SYI, totaling 0.13 $\pm$ 0.05 m.

We calculated season-long melt rates (**Table 1**), as well as monthly melt rates in the same manner as growth rates, though in addition to basal change we also considered change at the surface. Thus, for each stake, time-averaged basal melt rate was calculated as $\frac{h_b(t=1)-h_b(t=0)}{t_1-t_0}$, surface melt rate as $\frac{h_0(t=1)-h_0(t=0)}{t_1-t_0}$, and total melt rate as $\frac{H_1-H_0}{t_1-t_0}$, where h_b is the bottom position and h_0 is the surface position. Percent uncertainties can then be calculated as $\frac{\delta h_0+\delta h_b}{\Delta H}+\frac{\delta t}{\Delta t}$, where ΔH is the measured thickness change and $\delta h_0 = 0.01$, or twice the surface interface detection uncertainty. During the melt season, ΔH was on the order of 0.06 m, Δt on the order of 3 days, and δt approximately $\pm$4 hours. With these values we find uncertainties in the melt rates presented in **Figure 5b** of around 39%.

Average total ice melt rates were 0.013 m day^{-1} (0.012 m day^{-1} surface, 0.001 m day^{-1} bottom) in the week preceding June 30, and increased to 0.029 m day^{-1} (0.021 m day^{-1} surface, 0.008 m day^{-1} bottom) by July 24 (**Figure 5b**). Melt rates were highly variable between stakes during the melt season, with standard deviations of up to about 0.02 m day^{-1}. Variability in surface melt comprised most of the total melt variability and correlated strongly with net incident shortwave radiation ($R = 0.84$, $P = 0.018$) governed by albedo.

3.3.2. Meltwater production

We calculated a time series of the cumulative meltwater equivalent produced by ice and snow melt (**Figure 6**) according to Equations 1–3. The cumulative meltwater equivalents produced by surface ice melt (H_0), basal ice melt (H_b), and snow melt (H_s) are the cumulative sum of average thickness changes between each measurement interval of the ice surface ($\overline{\Delta h_0}$), ice bottom ($\overline{\Delta h_b}$), and snow ($\overline{\Delta h_s}$), multiplied by their respective densities. These averages were calculated as the mean of all operating stakes in each time interval, irrespective of ice type. Ice and snow densities were determined as the average of each parameter during Leg 4 (June 19–July 31, 2020): $\rho_i = 0.9$ g cm^{-3} (Oggier et al., 2023a; 2023b), and $\rho_s = 0.42$ g cm^{-3} (Macfarlane et al., 2021). Total cumulative meltwater equivalent (H_t) is the sum of the three terms: $H_t(t) = H_0(t) + H_b(t) + H_s(t)$

$$H_0(t) = \rho_i \sum_0^t \overline{\Delta h_0} \quad (1)$$

$$H_b(t) = \rho_i \sum_0^t \overline{\Delta h_b} \quad (2)$$

$$H_s(t) = \rho_s \sum_0^t \overline{\Delta h_s} \quad (3)$$

The contributions to meltwater production from ice surface, bottom, and snow melt were proportional to the melt observed in each category. Surface meltwater equivalent increased steadily over the season. Snow melt initially produced slightly more meltwater equivalent than bottom melt. The contribution from snow melt (approximately 0.09 m cumulative meltwater equivalent) remained unchanged following the completion of snow melt at most stakes in early July. Average bottom melt rate increased after July 19, at which point the cumulative meltwater produced by basal melt surpassed that of snow melt. Total meltwater equivalent reached 0.77 m by July 25. Ice surface melt composed the majority (74%), followed by bottom melt (14%) and snow melt (12%).

3.3.3. Melt ponds

Approximately 38% of stakes measured during the melt season had surface melt ponding at some point. Melt ponds occurred at more FYI stakes (9 of 18, 50%) than SYI stakes (3 of 9, 33%). The combined melt pond fraction was 4% at the beginning of observations (June 26) and increased throughout observations, peaking at 23% in the week of July 24. The timing and magnitudes of our melt

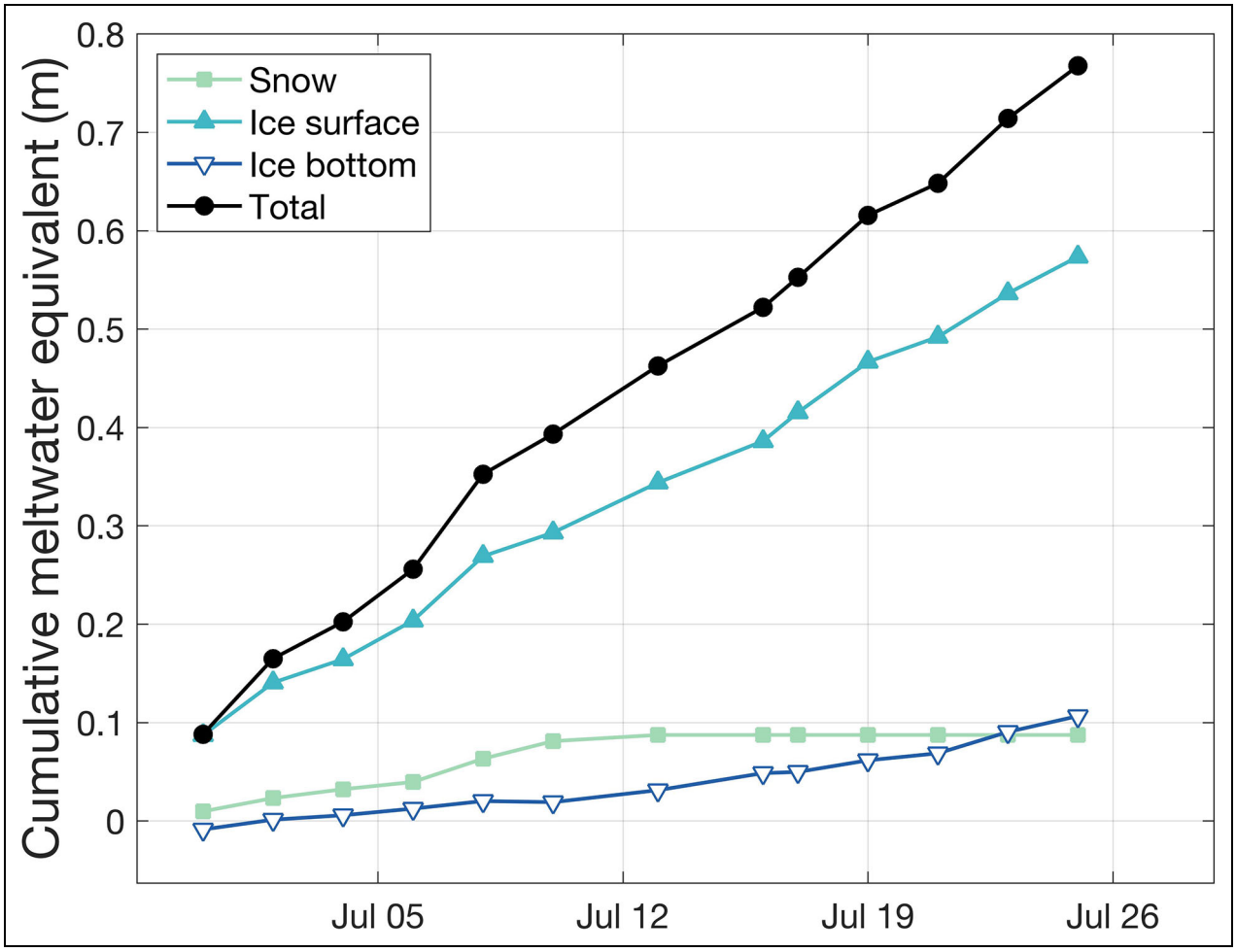

Figure 6. Cumulative meltwater equivalent during the ice melt season in 2020. We calculated cumulative meltwater equivalent according to Equations 1–3, shown here as time series traces for snow, ice surface, ice bottom, and total meltwater equivalent. Meltwater equivalent reflects the average cumulative snow and ice melt through the season, scaled by the appropriate densities. Total meltwater equivalent is the sum of snow, ice surface, and ice bottom meltwater equivalents.

pond fraction estimates agree with Niehaus et al. (2023). Though work by Webster et al. (2022) shows an earlier peak melt pond fraction, a disagreement is reasonable because their observations were made solely along the floe perimeter where early pond drainage by lateral overflow was likely.

Pond depths averaged between 0.12 m and 0.37 m over the season. Ponded ice exhibited surface melt rates that were between 1.5 and 15 times higher than unponded ice. The difference was generally largest at the beginning of the melt season, when unponded areas were still snow-covered. Basal melt rates at ponded stakes were also consistently, though only slightly, higher than at unponded stakes (mean difference of -0.001 m day^{-1}).

3.3.4. False bottoms

We observed false bottoms beginning in early summer (June 26) at the *Reunion Stakes* FYI site located in the interior of the floe. We noted false bottoms at *Reunion Stakes* beginning when we installed the site on June 26, and observed them until the end of our observations on the floe on July 31. Eight of the 9 stakes at *Reunion Stakes* exhibited false bottoms. The fraction of stakes at this site (about 90%) exhibiting false bottoms remained nearly unchanged during the summer melt observations. False bottoms were just beginning to deteriorate at the end of the campaign. We did not observe false bottoms at any SYI stakes (*Beanpole Stakes*), nor at the FYI site at the edge of the floe (*Drone Bones*). The thickness of the false bottoms ranged from 0.02 m to 0.08 m thick, and they were offset from the bottom of the ice by a water layer 0.16 m to 0.29 m thick.

3.4. Snow–ice interface temperature observations

Snow–ice interface temperatures (**Figure 7**) can be used to constrain the heat flux occurring through the snow and ice, particularly at times when temperature gradients through the snow and ice are temporally stable and approximately linear. At most stakes, snow–ice interface temperatures remained between -20°C and -12°C during most of the observed growth season. Stake 17 at the FYI *Stakes 1* site exhibited a much higher snow–ice

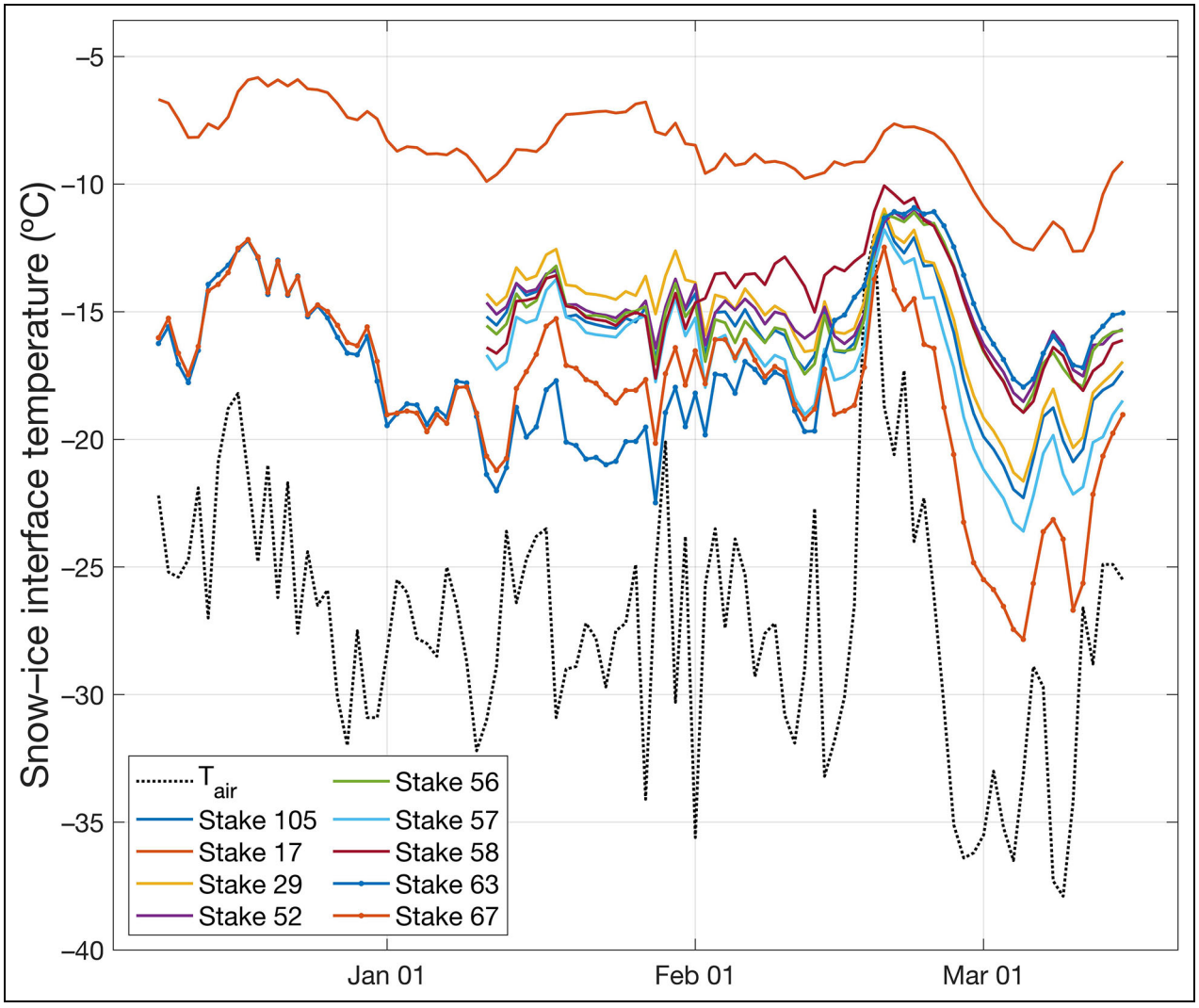

Figure 7. Selected snow–ice interface temperatures during the ice growth season in 2019–2020. Time series traces of snow–ice interface temperatures from a selection of first-year ice stakes at the *Ridge Ranch* and *Stakes 1* sites are shown. The 2 m air temperature is shown as the dashed black trace. All temperatures are smoothed using a 1-day moving average.

interface temperature due to thin ice (initial thickness of 0.26 m) and deep snow (0.41–0.48 m) at the stake, with temperatures 2–9°C warmer than the other stakes during the growth season. The relative behavior of each stake remained fixed (i.e., relatively cold sites remained colder throughout winter) with the exception of Stake 63, where a doubling of snow depth (from 0.10 m to 0.21 m) caused a significant increase in average temperature around February 14. There was a large temperature transition between February 18 and March 5, when the interface temperature first increased by about 5°C and then decreased by 8–12°C at all stakes, reaching a minimum of −28°C at Stake 67. The rapid temperature change coincided with a powerful low-pressure system traversing the area, and a subsequent period of deep cold under atmospheric inversions, during which 2 m air temperatures reached a low near −40°C (Shupe et al., 2022). Interface temperatures generally increased afterward, returning to the same −8°C to −12°C range for another month. We truncated the interface temperature time series to March 15, after which solar radiation adds additional complexity to interpreting these data in the context of thermodynamic mass balance.

4. Discussion

4.1. Ice growth on the Transpolar Drift

Prior studies have commented on the ice-thickness/ice-growth feedback loop (Bitz and Roe, 2004; Goosse et al., 2018; Petty et al., 2018; Zhang, 2021); as sea ice thins, conductive heat flux through the ice increases (Maykut, 1986). With equal thermodynamic forcing, a thinner ice pack should experience more growth over the winter than a thicker ice pack, creating a stabilizing (negative) feedback loop. Model studies have reproduced the predicted increase in ice growth as Arctic sea ice thins, but few studies have confirmed this trend in real-world observations. Previous work on this topic has been limited by the high uncertainty of thickness retrieval methods using satellite freeboard and submarine draft measurements (Zhang, 2021).

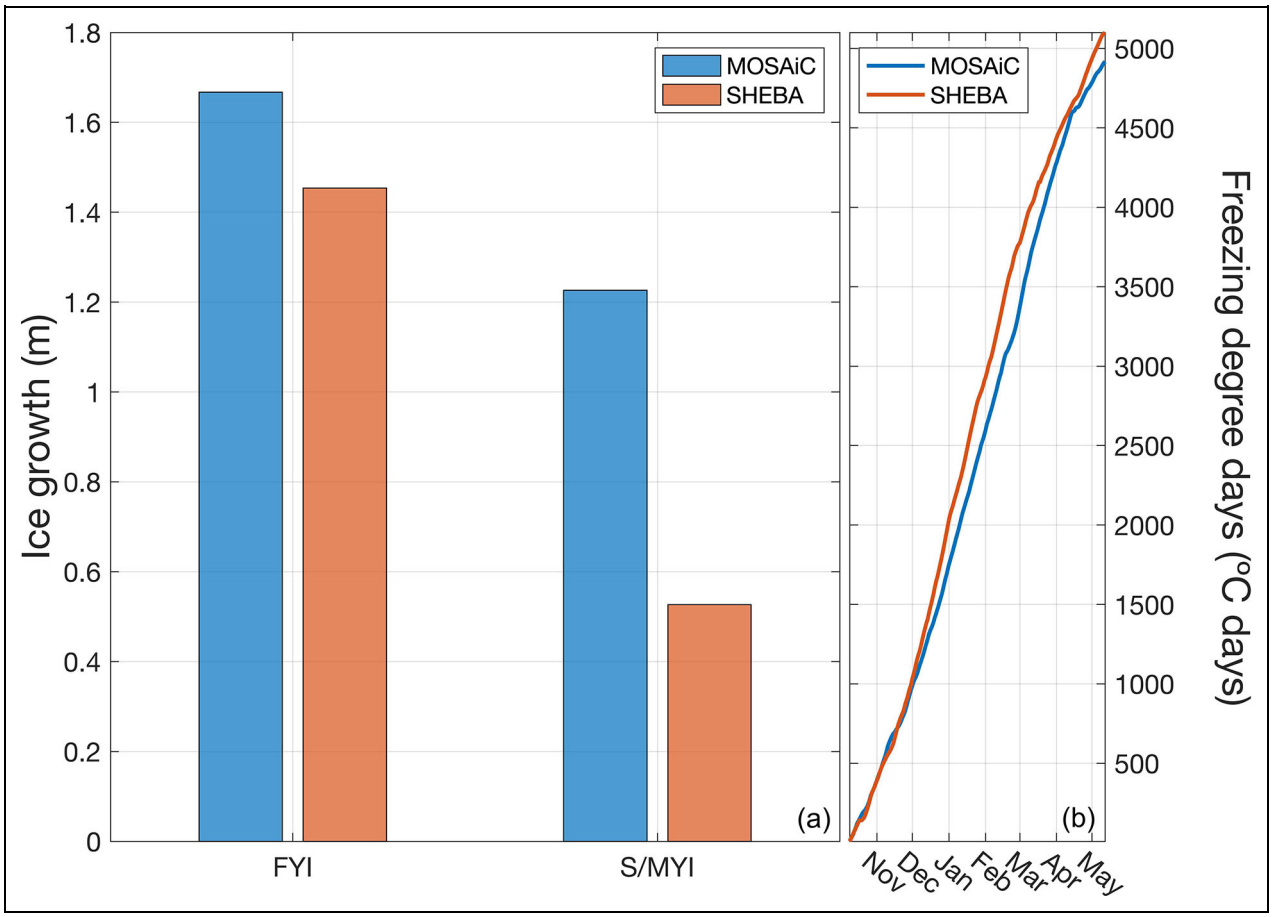

Figure 8. Total growth for first-year ice and second-year/multi-year ice on MOSAiC and SHEBA. Panel (a) shows average total growth for first-year ice (FYI) and second-year/multi-year ice (S/MYI) stakes on MOSAiC (blue) and SHEBA (orange). The S/MYI category includes only SYI for MOSAiC, and both SYI and MYI for SHEBA. Panel (b) shows freezing degree days calculated for MOSAiC (blue) and SHEBA (orange) between October 9 and May 12 of their respective years, 2019–2020 and 1997–1998.

Our results show greater winter sea ice growth on MOSAiC than observed in historical observations in the central Arctic. We compared ice growth in FYI and SYI categories on MOSAiC to FYI and MYI stake measurements on SHEBA (**Figure 8a**). On average, SYI grew 0.7 m more during the MOSAiC growth season than MYI on SHEBA. We determined a time series of freezing degree days (FDD) for MOSAiC and SHEBA according to Maykut (1986) (**Figure 8b**). FDD on MOSAiC increased in line with SHEBA through December, at which point MOSAiC began to lag SHEBA by up to approximately 380°C FDD through the midwinter. The two records then reapproached each other, nearly meeting on April 13, after which they again diverged slightly. MOSAiC reached approximately 4900°C FDD on May 12, while SHEBA reached approximately 5100°C FDD by the same date. Clearly FDD were similar for both expeditions and cannot explain the greater SYI growth on MOSAiC. Here (**Figure 8**), we calculated FDD beginning on the same date (October 9). While surface freeze-up began earlier at SHEBA (likely in late August or early September based on the 1998 freeze-up date noted in Perovich et al., 2003), MYI basal growth did not begin until the cold-front propagated through the ice, reaching the bottom in early November (Perovich et al., 2003). However, the longer SHEBA growth season and potentially higher FDD only serve to accentuate our conclusion: despite a shorter growth season and slightly lower FDD, both FYI and SYI ice at MOSAiC grew more than at SHEBA.

We asked whether shallower snow depth and thinner initial ice thickness could explain the greater SYI growth observed on MOSAiC. MOSAiC SYI stakes had a median initial thickness of 0.66 m at installation, compared to the SHEBA MYI median of 1.64 m. We used the Icepack single-column model (Hunke et al., 2023) to explore this question. SYI model runs were initialized on November 28 (the beginning of MOSAiC stake observations) and ended on May 12 (the end of ice growth observed at MOSAiC) so that the observational periods fully overlapped. We used average ice thickness and median snow depth values measured at MOSAiC and SHEBA stakes in a 5-day window around November 28 to initialize the respective model runs. Initial values for MOSAiC SYI were 0.80 m for ice thickness and 0.08 m for snow depth. For SHEBA MYI, these values were 1.76 m and 0.24 m, respectively. We used snow depth observations from stake measurements at each expedition to model time-resolved snow accumulation. MOSAiC observations were used for all oceanic and atmospheric model forcings (Long et al., 2019; Cox et al.,

2023a; 2023b; 2023c; 2023d; Schulz et al., 2023). Besides snow conditions and initial ice thickness, we used identical forcings for MOSAiC and SHEBA model runs. We did not use dynamic forcings for any Icepack simulations as we were comparing to stake results, which can only measure thermodynamic change.

The model simulated 1.03 m of ice growth for MOSAiC SYI, which aligns well with the average 1.00 m of growth observed from November 28 to May 12 at MOSAiC stakes. Stake observations from SHEBA show 0.41 m of average SYI growth during this period, 0.59 m less than at MOSAiC. The model simulated 0.76 m of ice growth for SHEBA MYI, 0.27 m less than the MOSAiC model growth and 0.35 m more than observed in SHEBA stake measurements. Thus, initial thickness and differences in snow depth and accumulation can explain 0.27 m (46%) of the 0.59 m difference in observed MOSAiC and SHEBA S/MYI growth. The remainder is likely due to higher ocean heat flux on SHEBA, which becomes a more significant term as snow and ice thickness increase and total conductive heat flux decreases (Maykut, 1986). Clearly, ice thickness and snow depth play a substantial role in SYI growth, and the thinning of S/MYI leads to greater ice production, partially stabilizing ice loss. However, further work is necessary to close the energy balance and fully explain the higher ice growth observed on MOSAiC in comparison to SHEBA.

Krumpen et al. (2019) indicate that surface warming in the Siberian sector of the Arctic is resulting in reduced ice thickness and concentration in the region, as well as lower volumes of ice advected out of the Siberian sector into the TD. Sumata et al. (2023) found a similar long-term decrease in ice concentration and age in the ice-formation zones of the Siberian Arctic. They observed a stepwise decrease in mean residence time in these areas from 15 to 6 months, which occurred after the 2007 sea ice minimum. This decrease in residence time means that ice advected from these areas is now primarily FYI, corresponding to lower initial ice volume, age, and thickness along the TD. Sumata et al. (2023), as well as Belter et al. (2021), further found that ocean heat flux in the Siberian sector is thinning sea ice before it begins its drift on the TD. Subsequently, faster drift leads to shorter and fewer growth seasons (as more FYI exits the TD before transitioning to SYI), preventing potential ice growth from fully compensating for initial thinning. Both found a negative trend in ice thickness in the Fram Strait and Greenland Sea areas, which Belter et al. (2021) attribute to shorter growth seasons resulting from increased TD speed. Our results indicate that the observed thinning prior to advection, as well as faster TD drift speeds, could be partially stabilized by an ice-thickness/ice-growth feedback loop. Although ice along the TD is experiencing a net thinning, this thinner ice demonstrates the potential to grow more and faster, damping the effect of surface ocean warming and reduced residence times in the TD and ice-formation areas. However, modeling studies show that the ice-thickness/ice-growth feedback will likely be overwhelmed by surface warming and cloud feedbacks in the future (Petty et al., 2018).

FYI grew an average of 0.22 m more on MOSAiC than SHEBA (**Figure 8a**). Because all FYI necessarily starts with the same initial thickness (0 m), this difference cannot be due to a thickness feedback mechanism. The similar FDD time series shows that differences in atmospheric temperature do not account for higher FYI growth on MOSAiC. We used the same modeling approach to explore whether thinner snow cover on MOSAiC FYI significantly increased conductive heat flux and resulted in greater FYI growth on MOSAiC. MOSAiC FYI had a median initial snow thickness of 0.02 m around November 28. SHEBA had a median initial snow thickness of 0.11 m on October 29. By the end of May, MOSAiC had a median snow thickness of 0.23 m, and SHEBA, 0.37 m.

We conducted Icepack model runs for November 28–May 12 (MOSAiC) and October 29–May 12 (SHEBA). We used average measured FYI thickness (0.28 m MOSAiC, 0.46 m SHEBA) to initialize the model runs. The MOSAiC model run simulated that FYI reached a thickness of 1.73 m by May 12, showing reasonable agreement with the observed average of 1.67 m. The SHEBA run simulated an average thickness on May 12 of 1.64 m, 0.32 m greater than the observed average of 1.32 m. Therefore, thinner initial cover snow and lower accumulation on MOSAiC explains 0.09 m (41%) of the 0.22 m greater growth seen in MOSAiC FYI. Like the SYI case, ocean heat flux may explain the remainder of the difference in growth, but further work is needed to explore this hypothesis.

Our results differ slightly from MOSAiC IMB results from Lei et al. (2022). They found slightly lower total ice growth (0.64–1.38 m, average of 0.92 $\pm$ 0.28, n = 10), noting that total growth depended primarily on initial thickness (0.35–1.80 m, average of 0.96 $\pm$ 0.48 m, n = 23). We suggest that our observations of higher ice growth (1.23 m SYI, 1.67 m FYI) are attributable to our thinner observed initial conditions (median 0.66 m).

While we focused solely on thermodynamic growth, dynamic growth also makes a significant contribution to winter ice growth and thickening. Von Albedyll et al. (2022) found a 30% contribution during the MOSAiC year, which will likely increase as ice thins and deforms more readily (Rampal et al., 2009; Itkin et al., 2017).

4.2. Effective thermal conductivity of snow

In considering the greater ice growth observed on MOSAiC compared to SHEBA, we asked whether higher snow thermal conductivity led to greater ice growth on MOSAiC. The effective thermal conductivity of snow on Arctic sea ice (k_s^*) is a critical parameter in sea ice thermodynamics. Despite its importance and variability, there are few available in situ estimates of k_s^*. Sturm et al. (2002) inferred k_s^* from ice growth and temperature measurements at several sites on SHEBA, finding a range of values, 0.168–0.699 W m^{-1} K^{-1}, with an average of 0.33 W m^{-1} K^{-1}. We derived estimates for k_s^* during the growth season on MOSAiC (**Figure 9**) using ice and snow thickness, snow–ice interface temperature, and air temperature data. We assumed linear, quasi steady-state temperature profiles

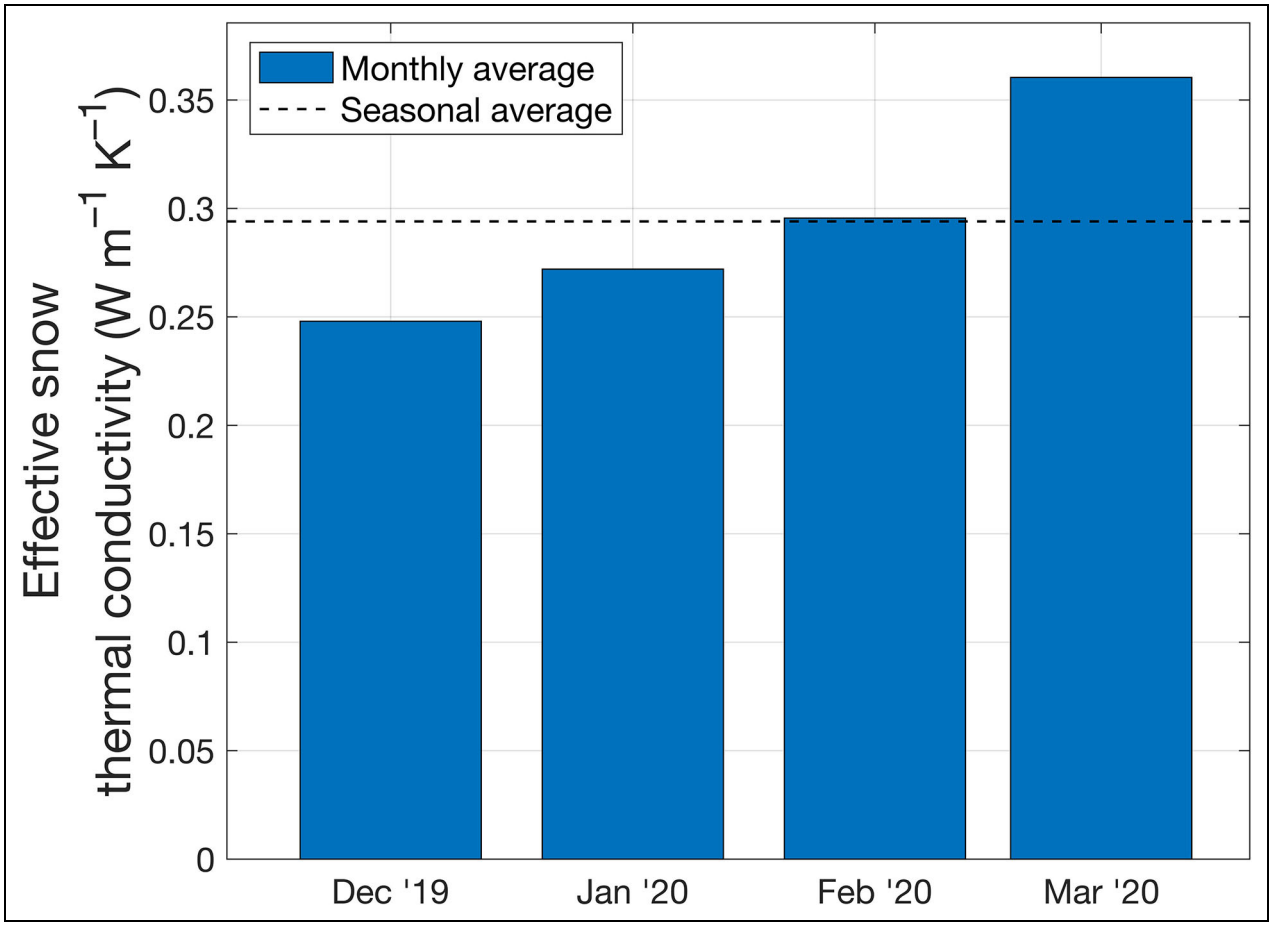

Figure 9. Effective thermal conductivity of snow during the winter season. Estimates of the effective thermal conductivity of snow (k_s^*) are shown as monthly averages of daily population medians throughout the winter (blue bars). The seasonal average is shown as the dashed horizontal line.

from the snow surface to the snow–ice interface and from the snow–ice interface to the ice bottom. We used Fourier's Law of heat conduction with linear temperature gradients to describe conductive heat flux through the ice and snow, and assumed that the flux through the ice was equal to the flux through the snow (Equation 4). Rearranging Equation 4 to solve for k_s^* is straightforward.

$$k_i \frac{T_0 - T_f}{h_i} = k_s^* \frac{T_0 - T_s}{h_s} \quad (4)$$

The snow–ice interface temperature (T_0) was taken from temperature sensors at the snow ice interface of selected stakes (Section 3.4), and was smoothed from hourly to daily average values. T_f is the ice–ocean interface temperature (assumed to be -1.8°C, the freezing point of seawater), and T_s is the snow surface temperature. We replaced T_s with the 2 m air temperature in all calculations. We note that periods of large, rapid temperature change violate the steady-state assumption and result in non-linear temperature profiles. Such temperature changes occurred several times during the analysis period; we did not attempt to correct for this effect. We recommend additional work to understand the impact of transient surface temperature when using this method. The thermal conductivity of the ice (k_i) was set at 2 W m^{-1} K^{-1} after Perovich et al. (2003). Ice and snow thicknesses (h_i, h_s) were taken from the stake associated with each snow–ice interface temperature sensor and were interpolated linearly to 1-day intervals.

We first calculated daily values for k_s^* at each stake, then found the median of the values at all stakes for each day. Finally, we took the monthly average and seasonal average of the medians. We only present results prior to sunrise so that we may neglect the influence of incoming shortwave radiation. We also neglect the heat sink term due to internal temperature change in the ice and snow.

We found a range of k_s^* over the season of 0.26–0.35 W m^{-1} K^{-1}, with a seasonal average of 0.29 W m^{-1} K^{-1}. This value agrees with SHEBA observations (Sturm et al., 2002); we therefore find that our data do not support the hypothesis that differences in effective snow thermal conductivity played a significant role in the greater ice growth observed at MOSAiC.

Our estimate also agrees with MOSAiC observations made by Macfarlane et al. (2023), while preliminary MOSAiC work by Sledd et al. (2022) and Perovich et al. (2023) shows higher values, in the range of 0.33–0.41 W m^{-1} K^{-1}. We observed an increase in k_s^* over the season, which we believe is due primarily to snow densification over the season, as observed by Macfarlane et al. (2023). We also saw an increase in snow depth anisotropy on short length scales (approximately 0.5 m) at several stakes in the dataset, which

may have resulted in significant lateral heat transfer, increasing the apparent (vertical) snow thermal conductivity. Further investigation is necessary to determine the sources of spatial and temporal variability in k_s^*, especially the influence of highly heterogeneous snow depth.

4.3. Increased ice melt on MOSAiC

Numerous studies have highlighted the decline in Arctic-wide sea ice extent, thickness, and volume over the modern observational record (e.g., Meier, 2017; Kwok, 2018). In addition to the factors discussed in Section 4.1, Stroeve et al. (2014) indicate that this decline is also due in large part to changes in the melt season. However, Stroeve and Notz (2018) noted that whether increased sea ice melt is the result of magnified atmospheric or oceanic heat exchange is not clear. To determine the magnitude and causes of increased summer ice melt, we compared stake data to historical ice mass balance buoy data.

As part of the North Pole Environmental Observatory (NPEO) project, ice mass balance buoys were deployed in the North Pole region each spring from 2000 to 2015 (Perovich et al., 2014). We compared MOSAiC observations in 2020 to data from the 11 NPEO buoys deployed between 2004 and 2015 that followed drift tracks similar to that of the MOSAiC floe. Substantially more total melt (0.35 m more melt) occurred on MOSAiC than on average in NPEO data (**Figure 10**). Most of the difference resulted from increased surface melt (mean of 0.50 m on MOSAiC, 0.18 m from NPEO, for a difference of 0.32 m). Perovich et al. (2008), and then others (Polyakov et al., 2012; Wang et al., 2016; Stroeve and Notz, 2018), found that increased solar heat deposition into the upper ocean is a strong driver of increased ice melt, ultimately through basal melting. Over the observed portion of the melt season, basal melt averaged 0.12 m at MOSAiC and 0.07 m at NPEO. MOSAiC thus showed more basal melt than NPEO, though the ranges were similar, and basal melt composed only a modest fraction of total melt for both during this period. We also note that the majority of basal melt in NPEO measurements occurred in the latter half of the melt season (approximately August–mid-September), a period which could not be considered in this comparative analysis. Because of its high drift speed (Belter et al., 2021), the MOSAiC floe exited the TD into Fram Strait and

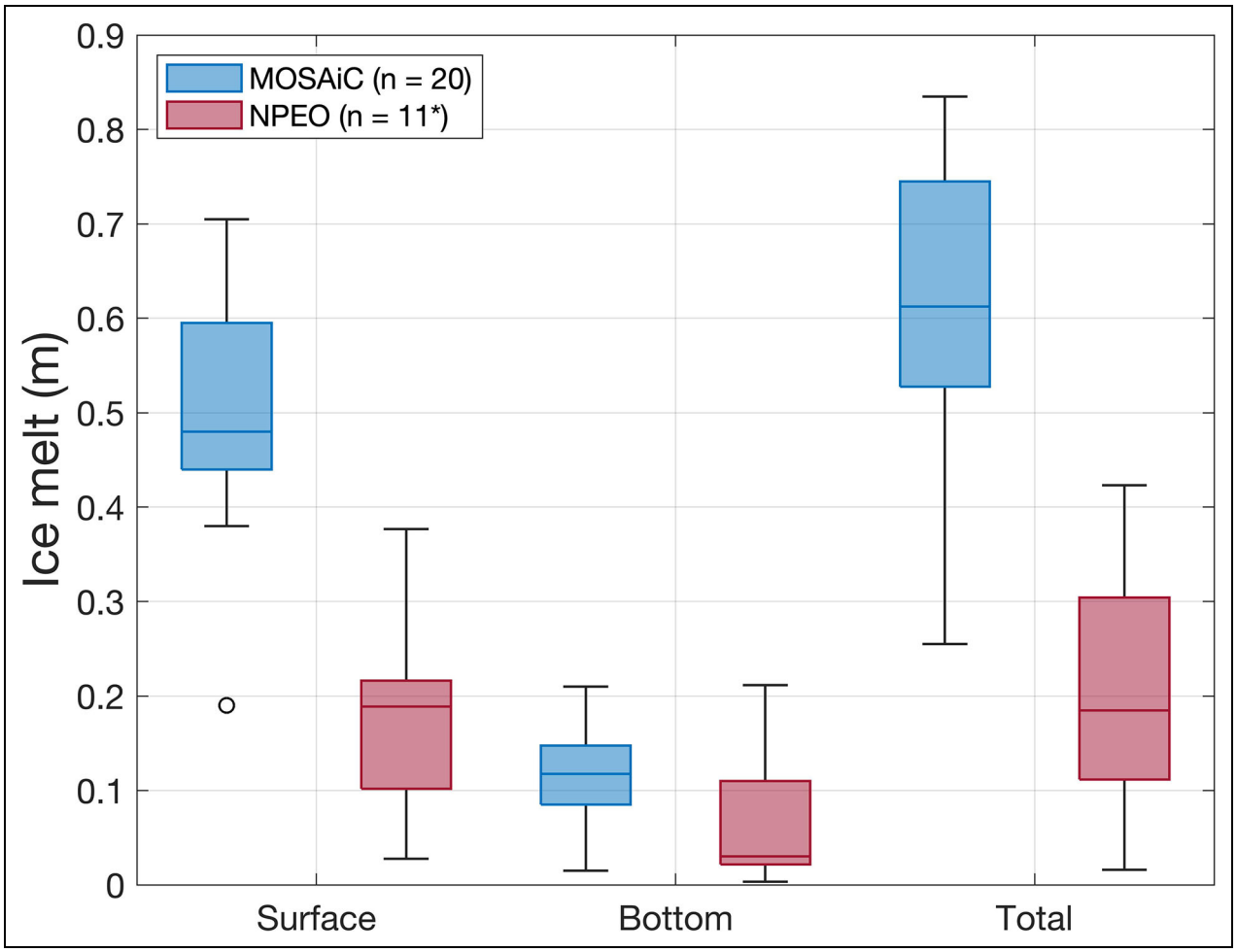

Figure 10. Comparative ice melt at MOSAiC (2020) and NPEO (2004–2015). The distribution of ice melt at MOSAiC stakes in 2020 and 11 NPEO buoys spanning 2004–2015 is shown in box and whisker plots. Medians are shown as the line inside each box. Lower and upper quartiles are the top and bottom edges of each box. The whiskers indicate the lowest and highest values in each range. Outliers are marked as open circles. Sample sizes are noted in parentheses in the legend. *NPEO sample size was n = 11, except for bottom melt, where n =10.

disintegrated before an increase in basal melt due to solar deposition would have become fully evident, that is, the record was truncated before we could fully test a hypothesis about changes in basal melt. Finally, observational and modeling studies have demonstrated that melt ponds tend to increase basal melt (Skyllingstad and Paulson, 2007; Flocco et al., 2012; Polashenski et al., 2012). While we observed a slight increase in basal melt at ponded stakes (mean 0.001 m day^{-1} higher than at unponded stakes), this effect did not significantly increase total basal melt in our observations.

Perhaps the most important observation of this mass-balance time series is the vulnerability of the ice under observation. The MOSAiC floe barely survived its first year, with a mean thickness at the end of the 2019 melt season of less than 0.5 m. Further, the ice observed at MOSAiC fully transited the Arctic during the 2019–2020 drift period, disintegrated in Fram Strait and likely melted completely, all in less than one year. Sumata et al. (2023) showed that mean TD transit times have decreased from 4.3 to 2.7 years, resulting in a significantly thinner ice cover. Here, a fundamental conclusion is that even ice that formed a year prior in the Siberian sector of the Arctic, the most upstream location in the TD, did not survive a full annual cycle. The accelerated life cycle of ice in the TD stands out as a marker of the changing Arctic ice cover.

At SHEBA, 135 stakes were installed, 95 survived the winter, and 68 lasted the entire year. In addition to impacting the continuity of results, the number of lost stakes is an indicator of the major changes in the state of the ice cover from earlier expeditions and is consistent with other indicators that the Arctic pack ice is drifting faster and deforming more readily than it once did (Kwok et al., 2013; Belter et al., 2021; Lei et al., 2022).

Thus, we highlight two factors that appeared to have driven a significant increase in sea ice melt on the MOSAiC floe compared to NPEO, both of which are related to increased drift speed along the TD. First, there was a large increase in surface melt that we hypothesize was due to a more southerly position caused by anomalously high TD speeds, which led to warmer air temperatures and greater incident solar radiation. Further investigation in the context of other MOSAiC observations is needed to confirm this hypothesis. Second, the increase in TD speed led to an earlier export of the MOSAiC floe into Fram Strait, and abrupt disintegration and melt in this area. Perovich et al. (2014) observed that, as of 2014, while there was widespread thinning across the Arctic, the North Pole/TD area was not experiencing as dramatic a change as the rest of the Arctic. They concluded that the "ice cover in this region is still robust at the end of the summer melt season." They also noted, however, that even though the ice in the region at that point survived summer melt, in all cases it subsequently entered Fram Strait and melted completely between the following December and March. Increased TD speeds have accelerated this process, leading to ice in the region entering Fram Strait and melting completely before the end of the melt season (Kwok et al., 2013; Belter et al., 2021; Lei et al., 2022). This acceleration, combined with intensified surface melt such as that seen on MOSAiC, will result in a less robust ice cover even at high latitudes. Sumata et al. (2022) recorded an unprecedented decline in sea ice volume export through Fram Strait in 2018, which they attributed to anomalous ice melt during January–March 2018. While they suggest that this decline was caused by low drift speeds increasing residence time in warm Atlantic water in Fram Strait, an additional probable cause is deeper infiltration of Atlantic water into the Arctic Ocean (Ingvaldsen et al., 2021).

Our observations represent only part of the melt season, but they show a significant increase in melt during the middle of the melt season compared to historical NPEO observations of the same period. We expect that increasing melt season duration and intensity (Stroeve et al., 2014) will only magnify this trend. Accelerating TD speeds threaten more rapid ice export into Fram Strait, less ice surviving into the following growth season, and an overall reduction in average Arctic ice thickness (Sumata et al., 2023). Further, as shown by Sumata et al. (2022), increased ice melt will likely still occur during periods of low TD speeds.

4.4. False bottoms and under-ice meltwater

As noted in Section 3.3, under-ice meltwater layers resulted in the formation of false bottoms at some FYI stakes. The formation of an under-ice meltwater layer and false bottom has opposing implications for ice mass balance: desalination and preconditioning for melt due to meltwater contact could potentially *increase* ice melt, while reduced contact with the underlying ocean mixed layer likely *decreases* bottom melt.

The stratified meltwater layer beneath the ice is likely at its freezing point, as it is bounded above by ice and below by either a false bottom or the colder, more saline mixed layer. Since the meltwater, which is no colder than its freezing point, has a lower salinity than the underlying mixed layer, the ice bottom is in contact with a warmer and fresher fluid than if it were in direct contact with the mixed layer. Eicken et al. (2002) showed that exposing the bottom of FYI to relatively warm, fresh meltwater causes desalination and internal melting, enlarging pore sizes and preconditioning the ice for rapid ablation later on.

On the other hand, the stratified meltwater layer and false bottom may isolate the sea ice from mixed layer water, which would ablate the ice bottom due to higher salinity and heat (Notz et al., 2003; Notz, 2005). The false bottom likely limits the turbulent transport of heat and salt to the ice bottom and may eliminate bottom ablation during the time that the false bottom is present. Finally, any solar heat deposited within the meltwater layer would be trapped there and result in ice bottom melt; however, little solar heat is likely absorbed in this relatively small freshwater layer.

The net impact seems to result in a reduction in bottom melt. A modeling study conducted by Smith (2019) predicts a 1%–8% reduction in ice melt when false bottoms are present. In situ observations on MOSAiC by Salganik et al. (2023a) agree with this prediction, finding an

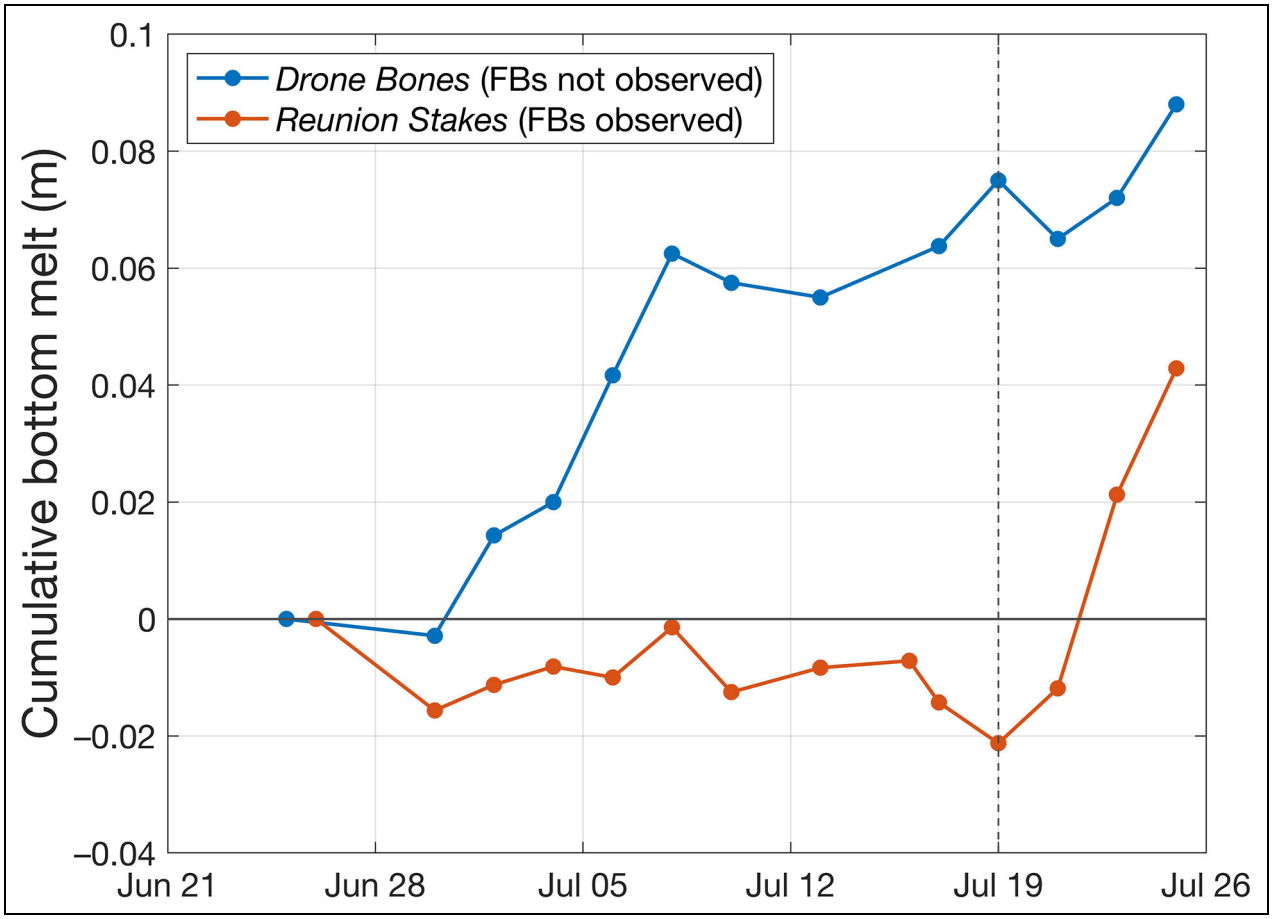

Figure 11. Cumulative ice bottom melt at sites *Reunion Stakes* and *Drone Bones* in 2020. Cumulative ice bottom melt is shown for two first-year ice sites throughout the melt season. *Reunion Stakes* (orange) was a first-year ice site at the interior of the floe, where false bottoms (FBs) were observed at approximately 90% of the stakes throughout the time series. *Drone Bones* (blue) was a first-year ice site at the edge of the floe, where no FBs were observed. Values below 0 m (solid black line) indicate net ice growth. We observed deterioration of false bottoms at *Reunion Stakes* after July 19, indicated by the dashed vertical line.

approximate 8% reduction in basal ice melt. Given the complex and under-observed nature of these processes, we analyzed our data to determine the net impact of false bottoms and found a higher reduction in bottom melt than predicted by Smith (2019) or observed by Salganik et al. (2023a).

Reunion Stakes and *Drone Bones* were both FYI sites measured during the melt season. The sites had initial ice thicknesses of 1.58 ± 0.12 m and 1.95 ± 0.44 m, respectively. *Reunion Stakes* experienced extensive formation of false bottoms, while *Drone Bones* saw none. At *Reunion Stakes*, average ablation of the true ice bottom was near zero from June 21 to July 21 (**Figure 11**). At the time, false bottoms were observed at 8 of the 9 stakes at the site, for about 90% local coverage compared to the 20% floe-scale average areal fraction found by Smith et al. (2022) and the similar 21% coverage found by Salganik et al. (2023a). During this period modest ice growth may have occurred on the true ice bottom at *Reunion Stakes*. An average of 0.02 m of growth was seen between July 8 and July 10, just above the 0.01 m measurement precision threshold. Meanwhile, from June 21 to July 21, 0.08–0.10 m of bottom melt occurred at *Drone Bones*.

Once false bottoms began to deteriorate at *Reunion Stakes*, however, melt rates were substantially greater than at *Drone Bones*, consistent with preconditioning by contact with warm, low salinity water. Even with this accelerated melt, the cumulative (seasonal) melt rate at *Reunion Stakes* still did not match that of the site without false bottoms (*Drone Bones*), and *Reunion Stakes* experienced 51% less cumulative basal melt over the observational period. We note that Salganik et al. (2023a) found that thicker FYI melted faster than thinner FYI on MOSAiC. We were unable to control for this effect in our observations, which could have further increased the melt rates at *Drone Bones*. However, due to the timing and magnitude of the differences in total melt and melt rate, we believe that false bottoms played the central role in decreasing melt at *Reunion Stakes*. We recommend additional work observing the mass-balance effect of false bottoms between and within ice thickness classes to separate these effects.

On balance, the formation of false bottoms thus appears to result in reduced bottom melt. Further investigation is necessary to explore both the prevalence of this phenomenon and the magnitude and variability of its impact on ice mass balance across ice types.

5. Conclusions

We made precise measurements of sea ice growth and melt during the 2019–2020 MOSAiC experiment in the central Arctic. We estimate that SYI at MOSAiC had an average thickness at the end of the 2019 melt season of approximately 0.43 m. By the time SYI stakes were installed, we observed a median installation thickness of 0.66 m. FYI grew an average of 1.67 m, and SYI grew 1.23 m until growth ended around May 12, 2020. These values were 0.22 m and 0.70 m more than on SHEBA, despite similar FDD.

We determined that differences in snow thermal conductivity were unlikely to have led to greater MOSAiC ice growth. The seasonal average of our estimates of effective thermal conductivity, 0.29 W m^{-1} K^{-1}, is similar and consistent with estimates made at SHEBA (Sturm et al., 2002) as well as select MOSAiC observations (Macfarlane et al., 2023). However, further work is recommended to determine the influence of snow spatial heterogeneity and lateral heat flux on ice growth.

Modeling experiments using the single column Icepack model (Hunke et al., 2023) indicated that thin snow and ice conditions contributed substantially to greater ice growth at MOSAiC than at SHEBA. Lei et al. (2022) reached a similar conclusion that ice growth is determined primarily by initial ice thickness, and while they observed slightly less ice growth during the winter than seen in our results, the difference may be explained by the greater initial ice thicknesses at their observation locations. This ice-thickness/ice-growth negative feedback may temper recently observed thinning of Arctic sea ice, but is likely to be overwhelmed by surface warming and cloud feedbacks in the future (Petty et al., 2018).

Surface melt onset was observed around May 25, and observations of melt continued until the floe broke apart in Fram Strait on July 31. On average, MOSAiC sea ice experienced 0.6 m of total melt during the observed melt period, which was 0.35 m more than the average recorded during the same calendar period by 11 NPEO buoys deployed between 2004 and 2015. Most of the difference was due to higher surface melt. We suggest that greater surface melt was due to a more southerly floe position, resulting in higher air temperatures and greater incident radiation. We recommend further work to explore this hypothesis.

We calculated a time series of meltwater equivalent for use in future meltwater budget analyses and meltwater process studies (**Figure 6**). Relative meltwater contributions from snow, surface, and basal melt reflect the respective melt in each category and compare to NPEO values in a like manner given similar snow and ice densities. We note that there are several meltwater sources that we did not document in this study, including ridge melt (see Salganik et al., 2023b) for MOSAiC ridge melt observations and lateral floe melt. Perovich et al. (2021) present a useful method for developing meltwater budgets for MYI sea ice. Our results are intended to contribute to, but not constitute, additional meltwater studies.

Basal melt was significantly lower at a MOSAiC FYI site where false bottoms were consistently observed, compared to a FYI site where false bottoms were never observed. Our results show a greater reduction in basal melt than predicted by Smith (2019) or observed at MOSAiC by Salganik et al. (2023a). Additional measurements of false bottoms and the thermohaline conditions directly beneath the ice during the melt season are needed to further constrain the character and mass balance implications of false bottoms and under-ice meltwater.

In sum, our observations are indicative of a thinning ice cover that is growing more during the winter, transiting the Transpolar Drift more quickly, and melting faster than seen in historical observations. This pattern is consistent with diminishing mean annual pack ice thicknesses observed over the last several decades by Hansen et al. (2013), Mahoney (2018), and Meier et al. (2021), among others. As increasing summer melt forces a decline in ice thickness, a resultant increase in conductive flux through the thinner winter ice pack enables more growth. However, as long as melt outpaces growth, mean annual thickness will decrease, while oscillations around the mean (growth and melt) will increase, until thermodynamic forcings stabilize and an equilibrium thickness is reached (Maykut, 1986).

The mass balance results presented in this article are critical for interpreting coincident atmospheric and oceanic heat flux measurements made during MOSAiC. They will also permit data-driven initialization of single column and full-scale climate model simulations. We recommend further work to improve high precision observations of winter snow distribution and the ice–ocean boundary layer during the melt season.

Data accessibility statement

All of the stake data generated on MOSAiC and used in this article have been archived in the Arctic Data Center:

- Raphael et al. 2022. Measurements of sea ice point-mass-balance using hotwire thickness gauges and ablation stakes during the Multidisciplinary drifting Observatory for the Study of Arctic Climate (MOSAiC) Expedition in the Central Arctic (2019–2020). Arctic Data Center. DOI: https://dx.doi.org/10.18739/A2NK36626.
- Perovich et al. 2022. Measurements of ice mass balance and temperature from autonomous Seasonal Ice Mass Balance buoys in the Arctic Ocean, 2019–2020. Arctic Data Center. DOI: https://dx.doi.org/10.18739/A20Z70Z01.

NPEO buoy data are available at the Cold Regions Research and Engineering Laboratory Ice Mass Balance Buoy Program portal:

- Perovich et al. 2023b. Observing and understanding climate change: Monitoring the mass balance, motion, and thickness of Arctic sea ice. Available at http://imb-crrel-dartmouth.org.

SHEBA mass balance data are available at the Earth Observing Laboratory data archive:

- Perovich et al. 2007. Ice Mass Balance. Version 1.0. UCAR/NCAR—Earth Observing Laboratory. DOI: https://dx.doi.org/10.5065/D6H130DF.

Snow–ice interface temperature data have been archived in the Arctic Data Center:

- Raphael et al. 2024. Snow–ice interface temperatures from the Multidisciplinary drifting Observatory for the Study of Arctic Climate (MOSAiC) Expedition in the Central Arctic (2019–2020) [dataset]. Arctic Data Center. DOI: https://dx.doi.org/10.18739/A2MP4VQ0X.

IcePack forcing data from MOSAiC have been archived in the Arctic Data Center:

- Clemens-Sewall et al. 2024. Merged datasets for the Multidisciplinary drifting Observatory for the Study of Arctic Climate (MOSAiC) Central Observatory in the Arctic Ocean (2019–2020) [dataset]. Arctic Data Center. DOI: https://dx.doi.org/10.18739/A2GX44W6J.

Forcing data for SHEBA IcePack model runs are available in the supplemental data in the "MOSAiC_Raphael_snow_sheba_MDF_20191005-20201001.csv" (CSV) file or "SHEBA Icepack Snow.nc" (NetCDF) file.

Supplemental files

The supplemental files for this article can be found as follows:

MOSAiC_Raphael_snow_sheba_MDF_20191005-20201001.csv. (CSV)

SHEBA Icepack Snow.nc. (NetCDF) file.

Acknowledgments

Data used in this manuscript were produced as part of the international Multidisciplinary drifting Observatory for the Study of Arctic Climate (MOSAiC) with the tag MOSAiC20192020 and the Project_ID: AWI_PS122_00. We thank all people involved in the expedition of the Research Vessel *Polarstern* (Knust, 2017) during MOSAiC in 2019–2020 as listed in Nixdorf et al. (2021). We are especially grateful for the logistics team and the crew of FS *Polarstern* who enabled this scientific work. We thank Oguz Demir, Steven Fons, Jennifer Hutchings, Arttu Jutila, Amy Macfarlane, Ilkka Matero, Marc Oggier, David Wagner, and many others for their capable help in the field. We thank reviewer Andrew Mahoney, an anonymous reviewer, and editor-in-chief Jody Deming for their insightful feedback, which greatly improved the manuscript. We thank Liba Hladik for her faithful editorial and administrative assistance.

Funding

IAR, DKP, DCS, and CMP were supported by NSF OPP-1724540 and NSF OPP-1724424. PI was supported by RCN #287871 (SIDRiFT). RL was supported by the National Natural Science Foundation of China (41976219) and the Chinese program for MOSAiC funded by the CAA. MMS was supported by NSF OPP-1724467, OPP-1724748, and OPP-2138787. MW conducted this work under the NSF Project 2138786.

Competing interests

The authors declare that they have no conflict of interest.

Author contributions

Contributed to conception and design: IAR, DKP, CMP, DCS.

Contributed to acquisition of data: IAR, DCS, PI, MN, JR, MMS, MJ.

Contributed to analysis and interpretation of data: IAR, DKP, CMP, DCS.

Conducted Icepack modeling and analysis: DCS and IAR.

Drafted and/or revised the article: IAR drafted the manuscript, all authors contributed to writing and revisions.

Approved the submitted version for publication: All authors.

References

Belter, HJ, **Krumpen, T**, **von Albedyll, L**, **Alekseeva, TA**, **Birnbaum, G**, **Frolov, SV**, **Hendricks, S**, **Herber, A**, **Polyakov, I**, **Raphael, I**, **Ricker, R**, **Serovetnikov, SS**, **Webster, M**, **Haas, C.** 2021. Interannual variability in Transpolar Drift summer sea ice thickness and potential impact of Atlantification. *The Cryosphere* **15**(6): 2575–2591.

Bitz, CM, **Holland, MM**, **Weaver, AJ**, **Eby, M.** 2001. Simulating the ice-thickness distribution in a coupled climate model. *Journal of Geophysical Research: Oceans* **106**(C2): 2441–2463. DOI: https://dx.doi.org/10.1029/1999JC000113.

Bitz, CM, **Roe, GH.** 2004. A mechanism for the high rate of sea ice thinning in the Arctic Ocean. *Journal of Climate* **17**(18): 3623–3632.

Briegleb, BP, **Light, B.** 2007. A Delta-Eddington multiple scattering parameterization for solar radiation in the sea ice component of the community climate system model. No. UCAR/NCAR/TN-472+STR. University Corporation for Atmospheric Research. DOI: https://dx.doi.org/10.5065/D6B27S71.

Clemens-Sewall, D, **Cox, C**, **Schulz, K**, **Raphael, I**. 2024. Merged datasets for the Multidisciplinary drifting Observatory for the Study of Arctic Climate (MOSAiC) Central Observatory in the Arctic Ocean (2019–2020) [dataset]. Arctic Data Center. DOI: https://dx.doi.org/10.18739/A2GX44W6J.

Cox, C, **Gallagher, M**, **Shupe, M**, **Persson, O**, **Blomquist, B**, **Grachev, A**, **Riihimaki, L**, **Kutchenreiter, M**, **Morris, V**, **Solomon, A**, **Brooks, I**, **Costa, D**, **Gottas, D**, **Hutchings, J**, **Osborn, J**, **Morris, S**, **Preusser, A**, **Uttal, T.** 2023a. Met City meteorological and surface flux measurements (Level 2 Processed), Multidisciplinary Drifting Observatory for the Study of Arctic Climate (MOSAiC), central Arctic, October 2019–September 2020 [dataset]. Arctic Data Center. DOI: https://dx.doi.org/10.18739/A2TM7227K.

Cox, C, **Gallagher, M**, **Shupe, M**, **Persson, O**, **Grachev, A**, **Solomon, A**, **Ayers, T**, **Costa, D**, **Hutchings, J**, **Leach, J**, **Morris, S**, **Osborn, J**, **Pezoa, S**, **Uttal, T.** 2023b. Atmospheric surface flux station #30 measurements (level 2 processed), Multidisciplinary Drifting Observatory for the Study of Arctic Climate (MOSAiC), central Arctic, October 2019–September 2020 [dataset]. Arctic Data Center. DOI: https://dx.doi.org/10.18739/A2K649V1F.

Cox, C, **Gallagher, M**, **Shupe, M**, **Persson, O**, **Grachev, A**, **Solomon, A**, **Ayers, T**, **Costa, D**, **Hutchings, J**, **Leach, J**, **Morris, S**, **Osborn, J**, **Pezoa, S**, **Uttal, T.** 2023c. Atmospheric surface flux station #40 measurements (level 3 final), Multidisciplinary Drifting Observatory for the Study of Arctic Climate (MOSAiC), central Arctic, October 2019–September 2020 [dataset]. Arctic Data Center. DOI: https://dx.doi.org/10.18739/A25X25F0P.

Cox, C, **Gallagher, M**, **Shupe, M**, **Persson, O**, **Grachev, A**, **Solomon, A**, **Ayers, T**, **Costa, D**, **Hutchings, J**, **Leach, J**, **Morris, S**, **Osborn, J**, **Pezoa, S**, **Uttal, T.** 2023d. Atmospheric surface flux station #50 measurements (level 2 complete), Multidisciplinary Drifting Observatory for the Study of Arctic Climate (MOSAiC), central Arctic, October 2019–September 2020 [dataset]. Arctic Data Center. DOI: https://dx.doi.org/10.18739/A2251FM5R.

Cox, C, **Persson, OPG**, **Shupe, M**, **Solomon, A**, **Gallagher, M**, **Lawrence, Z**, **Perovich, D.** 2021. Driving mechanisms for the onset of the summer melt season at MOSAiC. AGU Fall Meeting Abstracts 2021, C55C-0603.

Eicken, H, **Krouse, HR**, **Kadko, D**, **Perovich, DK**. 2002. Tracer studies of pathways and rates of meltwater transport through Arctic summer sea ice. *Journal of Geophysical Research: Oceans* **107**(C10): SHE 22-1–SHE 22-20.

Eicken, H, **Tucker, WB**, **Perovich, DK.** 2001. Indirect measurements of the mass balance of summer Arctic sea ice with an electromagnetic induction technique. *Annals of Glaciology* **33**: 194–200.

Flocco, D, **Schroeder, D**, **Feltham, DL**, **Hunke, EC.** 2012. Impact of melt ponds on Arctic sea ice simulations from 1990 to 2007. *Journal of Geophysical Research: Oceans* **117**(C9): 1–17.

Goosse, H, **Kay, JE**, **Armour, KC**, **Bodas-Salcedo, A**, **Chepfer, H**, **Docquier, D**, **Jonko, A**, **Kushner, PJ**, **Lecomte, O**, **Massonnet, F**, **Park, HS**, **Pithan, F**, **Svensson, G**, **Vancoppenolle, M.** 2018. Quantifying climate feedbacks in polar regions. *Nature Communications* **9**(1): 1919.

Haas, C, **Lobach, J**, **Hendricks, S**, **Rabenstein, L**, **Pfaffling, A.** 2009. Helicopter-borne measurements of sea ice thickness, using a small and lightweight, digital EM system. *Journal of Applied Geophysics* **67**(3): 234–241.

Hansen, E, **Gerland, S**, **Granskog, MA**, **Pavlova, O**, **Renner, AHH**, **Haapala, J**, **Løyning, TB**, **Tschudi, M.** 2013. Thinning of Arctic sea ice observed in Fram Strait: 1990–2011. *Journal of Geophysical Research: Oceans* **118**(10): 5202–5221.

Hanson, AM. 1965. Studies of the mass budget of Arctic pack-ice floes. *Journal of Glaciology* **5**(41): 701–709.

Hunke, E, **Allard, A**, **Bailey, DA**, **Blain, P**, **Craig, A**, **Dupont, F**, **DuVivier, A**, **Grumbine, R**, **Hebert, D**, **Holland, M**, **Jeffery, N**, **Lemieux, JF**, **Osinski, R**, **Rasmussen, T**, **Ribergaard, M**, **Roach, L**, **Roberts, A**, **Turner, M**, **Winton, M.** 2023. CICE-Consortium/Icepack: Icepack 1.4.0 (1.4.0). Zenodo. DOI: https://dx.doi.org/10.5281/zenodo.10056496.

Hunke, E, **Lipscomb, W**, **Jones, P**, **Turner, A**, **Jeffery, N**, **Elliott, S.** 2017. CICE, the Los Alamos Sea Ice Model (No. CICE; 005315WKSTN00). Los Alamos, NM: Los Alamos National Lab (LANL).

Ingvaldsen, RB, **Assmann, KM**, **Primicerio, R**, **Fossheim, M**, **Polyakov, IV**, **Dolgov, AV.** 2021. Physical manifestations and ecological implications of Arctic Atlantification. *Nature Reviews Earth & Environment* **2**(12): 874–889.

Itkin, P, **Hendricks, S**, **Webster, M**, **von Albedyll, L**, **Arndt, S**, **Divine, D**, **Jaggi, M**, **Oggier, M**, **Raphael, I**, **Ricker, R**, **Rohde, J**, **Schneebeli, M**, **Liston, GE.** 2023. Sea ice and snow characteristics from year-long transects at the MOSAiC central observatory. *Elementa: Science of the Anthropocene* **11**(1): 00048. DOI: https://dx.doi.org/10.1525/elementa.2022.00048.

Itkin, P, **Spreen, G**, **Cheng, B**, **Doble, M**, **Girard-Ardhuin, F**, **Haapala, J**, **Hughes, N**, **Kaleschke, L**, **Nicolaus, M**, **Wilkinson, J.** 2017. Thin ice and storms: Sea ice deformation from buoy arrays deployed during N-ICE 2015. *Journal of Geophysical Research: Oceans* **122**(6): 4661–4674.

Koerner, RM. 1973. The mass balance of the sea ice of the Arctic Ocean. *Journal of Glaciology* **12**(65): 173–185.

Koo, Y, **Lei, R**, **Cheng, Y**, **Cheng, B**, **Xie, H**, **Hoppmann, M**, **Kurtz, NT**, **Ackley, SF**, **Mestas-Nuñez, AM.** 2021. Estimation of thermodynamic and dynamic contributions to sea ice growth in the Central Arctic using ICESat-2 and MOSAiC SIMBA buoy data. *Remote Sensing of Environment* **267**: 112730.

Krumpen, T, **Belter, HJ**, **Boetius, A**, **Damm, E**, **Haas, C**, **Hendricks, S**, **Nicolaus, M**, **Nöthig, EM**, **Paul, S**, **Peeken, I**, **Ricker, R**, **Stein, R.** 2019. Arctic warming interrupts the Transpolar Drift and affects long-range transport of sea ice and ice-rafted matter. *Scientific Reports* **9**(1): 5459.

Krumpen, T, **Birrien, F**, **Kauker, F**, **Rackow, T**, **von Albedyll, L**, **Angelopoulos, M**, **Belter, HJ**, **Bessonov, V**, **Damm, E**, **Dethloff, K**, **Haapala, J**, **Haas, C**, **Harris, C**, **Hendricks, S**, **Hoelemann, J**, **Hoppmann, M**, **Kaleschke, L**, **Karcher, M**, **Kolabutin, N**, **Lei, R**, **Lenz, J**, **Morgenstern, A**, **Nicolaus, M**, **Nixdorf, U**, **Petrovsky, T**, **Rabe, B**, **Rabenstein, L**, **Rex, M**, **Ricker, R**, **Rohde, J**, **Shimanchuk, E**, **Singha, S**, **Smolyanitsky, V**, **Sokolov, V**, **Stanton, T**, **Timofeeva, A**, **Tsamados, M**, **Watkins, D.** 2020. The MOSAiC ice floe: Sediment-laden survivor from the Siberian shelf. *The Cryosphere* **14**(7): 2173–2187.

Krumpen, T, **von Albedyll, L**, **Goessling, HF**, **Hendricks, S**, **Juhls, B**, **Spreen, G**, **Willmes, S**, **Belter, HJ**, **Dethloff, K**, **Haas, C**, **Kaleschke, L**, **Katlein, C**, **Tian-Kunze, X**, **Ricker, R**, **Rostosky, P**, **Rückert, J**, **Singha, S**, **Sokolova, J.** 2021. MOSAiC drift expedition from October 2019 to July 2020: Sea ice conditions from space and comparison with previous years. *The Cryosphere* **15**(8): 3897–3920.

Kwok, R. 2018. Arctic sea ice thickness, volume, and multiyear ice coverage: Losses and coupled variability (1958–2018). *Environmental Research Letters* **13**(10): 105005.

Kwok, R, **Spreen, G**, **Pang, S.** 2013. Arctic sea ice circulation and drift speed: Decadal trends and ocean currents. *Journal of Geophysical Research: Oceans* **118**(5): 2408–2425.

Lei, R, **Cheng, B**, **Heil, P**, **Vihma, T**, **Wang, J**, **Ji, Q**, **Zhang, Z.** 2018. Seasonal and interannual variations of sea ice mass balance from the central Arctic to the Greenland sea. *Journal of Geophysical Research: Oceans* **123**(4): 2422–2439.

Lei, R, **Cheng, B**, **Hoppmann, M**, **Zhang, F**, **Zuo, G**, **Hutchings, JK**, **Lin, L**, **Lan, M**, **Wang, H**, **Regnery, J**, **Krumpen, T**, **Haapala, J**, **Rabe, B**, **Perovich, DK**, **Nicolaus, M.** 2022. Seasonality and timing of sea ice mass balance and heat fluxes in the Arctic Transpolar Drift during 2019–2020. *Elementa: Science of the Anthropocene* **10**(1): 000089. DOI: https://dx.doi.org/10.1525/elementa.2021.000089.

Lipscomb, WH. 2001. Remapping the thickness distribution in sea ice models. *Journal of Geophysical Research: Oceans* **106**(C7): 13989–14000. DOI: https://dx.doi.org/10.1029/2000JC000518.

Long, C, **Ermold, B**, **Riihimaki, L**, **Hall, E.** 2019. Shipboard radiometer system. DOI: https://dx.doi.org/10.5439/1411966.

Macfarlane, AR, **Löwe, H**, **Gimenes, L**, **Wagner, DN**, **Dadic, R**, **Ottersberg, R**, **Hämmerle, S**, **Schneebeli, M.** 2023. Thermal conductivity of snow on Arctic sea ice. *EGUsphere*: 1–22.

Macfarlane, AR, **Schneebeli, M**, **Dadic, R**, **Wagner, DN**, **Arndt, S**, **Clemens-Sewall, D**, **Hämmerle, S**, **Hannula, HR**, **Jaggi, M**, **Kolabutin, N**, **Krampe, D**, **Lehning, M**, **Matero, I**, **Nicolaus, M**, **Oggier, M**, **Pirazzini, R**, **Polashenski, C**, **Raphael, I**, **Regnery, J**, **Shimanchuck, E**, **Smith, MM**, **Tavri, A.** 2021. Snowpit raw data collected during the MOSAiC expedition. PANGAEA. DOI: https://dx.doi.org/10.1594/PANGAEA.935934.

Mahoney, AR. 2018. Landfast sea ice in a changing Arctic. NOAA Arctic Report Card: 99. Available at https://lindseyresearch.com/wp-content/uploads/2021/12/NHTSA-2021-0053-1554-77-Osborne-2018_-ArcticReportCard.pdf#page=100. Accessed June 30, 2024.

Maslanik, JA, **Fowler, C**, **Stroeve, J**, **Drobot, S**, **Zwally, J**, **Yi, D**, **Emery, W.** 2007. A younger, thinner Arctic ice cover: Increased potential for rapid, extensive sea-ice loss. *Geophysical Research Letters* **34**(24): L24501.

Maykut, GA. 1986. The surface heat and mass balance, in Untersteiner, N ed., *The geophysics of sea ice*. Boston, MA: Springer: 395–463.

Meier, WN. 2017. Losing Arctic sea ice: Observations of the recent decline and the long-term context, in Thomas, DN ed., *Sea ice*. Hoboken, NJ: John Wiley & Sons, Inc.: 290–303.

Meier, WN, **Perovich, D**, **Farrell, S**, **Haas, C**, **Hendricks, S**, **Petty, AA**, **Webster, M**, **Divine, D**, **Gerland, S**, **Kaleschke, L**, **Ricker, R**, **Steer, A**, **Tian-Kunze, X**, **Schudi, M**, **Wood, K.** 2021. Sea ice. NOAA Technical Report OAR ARC; 21-05. Arctic Report Card 2021. Available at https://repository.library.noaa.gov/view/noaa/34474. Accessed June 30, 2024.

Meier, WN, **Stroeve, J**, **Fetterer, F.** 2007. Whither Arctic sea ice? A clear signal of decline regionally, seasonally and extending beyond the satellite record. *Annals of Glaciology* **46**: 428–434.

Nicolaus, M, **Perovich, DK**, **Spreen, G**, **Granskog, MA**, **Albedyll, LV**, **Angelopoulos, M**, **Anhaus, P**, **Arndt, S**, **Belter, HJ**, **Bessonov, V**, **Birnbaum, G**, **Brauchle, J**, **Calmer, R**, **Cardellach, E**, **Cheng, B**, **Clemens-Sewall, D**, **Dadic, R**, **Damm, E**, **de Boer, G**, **Demir, O**, **Dethloff, K**, **Divine, DV**, **Fong, AA**, **Fons, S**, **Frey, MM**, **Fuchs, N**, **Gabarró, C**, **Gerland, S**, **Goessling, HF**, **Gradinger, R**, **Haapala, J**, **Haas, C**, **Hamilton, J**, **Hannula, H-R**, **Hendricks, S**, **Herber, A**, **Heuzé, C**, **Hoppmann, M**, **Høyland, KV**, **Huntemann, M**, **Hutchings, JK**, **Hwang, B**, **Itkin, P**, **Jacobi, H-W**, **Jaggi, M**, **Jutila, A**, **Kaleschke, L**, **Katlein, C**, **Kolabutin, N**, **Krampe, D**, **Kristensen, SS**, **Krumpen, T**, **Kurtz, N**, **Lampert, A**, **Lange, BA**, **Lei, R**, **Light, B**, **Linhardt, F**, **Liston, GE**, **Loose, B**, **Macfarlane, AR**, **Mahmud, M**, **Matero, IO**, **Maus, S**, **Morgenstern, A**, **Naderpour, R**, **Nandan, V**, **Niubom, A**, **Oggier, M**, **Oppelt, N**, **Pätzold, F**, **Perron, C**, **Petrovsky, T**, **Pirazzini, R**, **Polashenski, C**, **Rabe, B**, **Raphael, IA**, **Regnery, J**, **Rex, M**, **Ricker, R**, **Riemann-Campe, K**, **Rinke, A**, **Rohde, J**, **Salganik, E**, **Scharien, RK**, **Schiller, M**, **Schneebeli, M**, **Semmling, M**, **Shimanchuk, E**, **Shupe, MD**, **Smith, MM**, **Smolyanitsky, V**, **Sokolov, V**, **Stanton, T**, **Stroeve, J**, **Thielke, L**, **Timofeeva, A**, **Tonboe, RT**, **Tavri, A**, **Tsamados, M**, **Wagner, DN**, **Watkins, D**, **Webster, M**, **Wendisch, M**. 2022. Overview of the MOSAiC expedition: Snow and sea ice. *Elementa: Science of the Anthropocene* **10**(1): 000046. DOI: https://dx.doi.org/10.1525/elementa.2021.000046.

Niehaus, H, **Spreen, G**, **Birnbaum, G**, **Istomina, L**, **Jäkel, E**, **Linhardt, F**, **Neckel, N**, **Fuchs, N**, **Nicolaus, M**, **Sperzel, T**, **Tao, R**, **Webster, M**, **Wright, N**. 2023. Sea ice melt pond fraction derived from Sentinel-2 data: Along the MOSAiC drift and Arctic-wide. *Geophysical Research Letters* **50**(5): e2022GL102102.

Notz, D. 2005. Thermodynamic and fluid-dynamical processes in sea ice [Doctoral dissertation]. Cambridge, UK: University of Cambridge.

Notz, D, **McPhee, MG**, **Worster, MG**, **Maykut, GA**, **Schlünzen, KH**, **Eicken, H.** 2003. Impact of

underwater-ice evolution on Arctic summer sea ice. *Journal of Geophysical Research: Oceans* **108**(C7): 3223.

Oggier, M, **Salganik, E**, **Whitmore, L**, **Fong, AA**, **Hoppe, CJM**, **Rember, R**, **Høyland, KV**, **Divine, DV**, **Gradinger, R**, **Fons, SW**, **Abrahamsson, K**, **Aguilar-Islas, AM**, **Angelopoulos, M**, **Arndt, S**, **Balmonte, JP**, **Bozzato, D**, **Bowman, JS**, **Castellani, G**, **Chamberlain, E**, **Creamean, J**, **D'Angelo, A**, **Damm, E**, **Dumitrascu, A**, **Eggers, SL**, **Gardner, J**, **Grosfeld, L**, **Haapala, J**, **Immerz, A**, **Kolabutin, N**, **Lange, BA**, **Lei, R**, **Marsay, CM**, **Maus, S**, **Müller, O**, **Olsen, LM**, **Nuibom, A**, **Ren, J**, **Rinke, A**, **Sheikin, I**, **Shimanchuk, E**, **Snoeijs-Leijonmalm, P**, **Spahic, S**, **Stefels, J**, **Torres-Valdés, S**, **Torstensson, A**, **Ulfsbo, A**, **Verdugo, J**, **Vortkamp, M**, **Wang, L**, **Webster, M**, **Wischnewski, L**, **Granskog, MA**. 2023a. First-year sea-ice salinity, temperature, density, oxygen and hydrogen isotope composition from the main coring site (MCS-FYI) during MOSAiC legs 1 to 4 in 2019/2020 [dataset]. PANGAEA. DOI: https://dx.doi.org/10.1594/PANGAEA.956732.

Oggier, M, **Salganik, E**, **Whitmore, L**, **Fong, AA**, **Hoppe, CJM**, **Rember, R**, **Høyland, KV**, **Divine, DV**, **Gradinger, R**, **Fons, SW**, **Abrahamsson, K**, **Aguilar-Islas, AM**, **Angelopoulos, M**, **Arndt, S**, **Balmonte, JP**, **Bozzato, D**, **Bowman, JS**, **Castellani, G**, **Chamberlain, E**, **Creamean, J**, **D'Angelo, A**, **Damm, E**, **Dumitrascu, A**, **Eggers, L**, **Gardner, J**, **Grosfeld, L**, **Haapala, J**, **Immerz, A**, **Kolabutin, N**, **Lange, BA**, **Lei, R**, **Marsay, CM**, **Maus, S**, **Olsen, LM**, **Müller, O**, **Nuibom, A**, **Ren, J**, **Rinke, A**, **Sheikin, I**, **Shimanchuk, E**, **Snoeijs-Leijonmalm, P**, **Spahic, S**, **Stefels, J**, **Torres-Valdés, S**, **Torstensson, A**, **Ulfsbo, A**, **Verdugo, J**, **Vortkamp, M**, **Wang, L**, **Webster, M**, **Wischnewski, L**, **Granskog, MA**. 2023b. Second-year sea-ice salinity, temperature, density, oxygen and hydrogen isotope composition from the main coring site (MCS-SYI) during MOSAiC legs 1 to 4 in 2019/2020 [dataset]. PANGAEA. DOI: https://dx.doi.org/10.1594/PANGAEA.959830.

Perovich, D, **Raphael, I**, **Moore, R**, **Clemens-Sewall, D**, **Lei, R**, **Sledd, A**, **Polashenski, C.** 2023a. Sea ice heat and mass balance measurements from four autonomous buoys during the MOSAiC drift campaign. *Elementa: Science of the Anthropocene* **11**(1): 00017. DOI: https://dx.doi.org/10.1525/elementa.2023.00017.

Perovich, D, **Raphael, I**, **Moore, R**, **Clemens-Sewall, D**, **Polashenski, C**, **Planck, C.** 2022. Measurements of ice mass balance and temperature from autonomous seasonal ice mass balance buoys in the Arctic Ocean, 2019–2020 [dataset]. Arctic Data Center. DOI: https://dx.doi.org/10.18739/A20Z70Z01.

Perovich, D, **Richter-Menge, J**, **Polashenski, C**. 2023b. Observing and understanding climate change: Monitoring the mass balance, motion, and thickness of Arctic sea ice. Available at http://imb-crrel-dartmouth.org.

Perovich, D, **Richter-Menge, J**, **Polashenski, C**, **Elder, B**, **Arbetter, T**, **Brennick, O**. 2014. Sea ice mass balance observations from the north pole environmental observatory. *Geophysical Research Letters* **41**(6): 2019–2025.

Perovich, D, **Richter-Menge, JA**. 2006. From points to poles: Extrapolating point measurements of sea-ice mass balance. *Annals of Glaciology* **44**: 188–192.

Perovich, D, **Smith, M**, **Light, B**, **Webster, M.** 2021. Meltwater sources and sinks for multiyear Arctic sea ice in summer. *The Cryosphere* **15**(9): 4517–4525. DOI: https://dx.doi.org/10.5194/tc-15-4517-2021.

Perovich, DK, **Grenfell, T**, **Light, B**, **Richter-Menge, J**, **Tucker, T**, **Eicken, H**. 2007. Ice Mass Balance. Version 1.0. UCAR/NCAR—Earth Observing Laboratory. DOI: https://dx.doi.org/10.5065/D6H130DF.

Perovich, DK, **Grenfell, TC**, **Richter-Menge, JA**, **Light, B**, **Tucker, WB III**, **Eicken, H**. 2003. Thin and thinner: Sea ice mass balance measurements during SHEBA. *Journal of Geophysical Research: Oceans* **108**(C3).

Perovich, DK, **Richter-Menge, JA**, **Jones, KF**, **Light, B**. 2008. Sunlight, water, and ice: Extreme Arctic sea ice melt during the summer of 2007. *Geophysical Research Letters* **35**(11).

Petty, AA, **Holland, MM**, **Bailey, DA**, **Kurtz, NT.** 2018. Warm Arctic, increased winter sea ice growth? *Geophysical Research Letters* **45**(23): 12922–12930.

Planck, CJ, **Whitlock, J**, **Polashenski, C**, **Perovich, D.** 2019. The evolution of the seasonal ice mass balance buoy. *Cold Regions Science and Technology* **165**: 102792.

Polashenski, C, **Perovich, D**, **Courville, Z.** 2012. The mechanisms of sea ice melt pond formation and evolution. *Journal of Geophysical Research: Oceans* **117**(C1).

Polyakov, IV, **Walsh, JE**, **Kwok, R.** 2012. Recent changes of Arctic multiyear sea ice coverage and the likely causes. *Bulletin of the American Meteorological Society* **93**(2): 145–151.

Rabe, B, **Heuzé, C**, **Regnery, J**, **Aksenov, Y**, **Allerholt, J**, **Athanase, M**, **Bai, Y**, **Basque, C**, **Bauch, D**, **Baumann, TM**, **Chen, D**, **Cole, ST**, **Craw, L**, **Davies, A**, **Damm, E**, **Dethloff, K**, **Divine, DV**, **Doglioni, F**, **Ebert, F**, **Fang, Y-C**, **Fer, I**, **Fong, AA**, **Gradinger, R**, **Granskog, MA**, **Graupner, R**, **Haas, C**, **He, H**, **He, Y**, **Hoppmann, M**, **Janout, M**, **Kadko, D**, **Kanzow, T**, **Karam, S**, **Kawaguchi, Y**, **Koenig, Z**, **Kong, B**, **Krishfield, RA**, **Krumpen, T**, **Kuhlmey, D**, **Kuznetsov, I**, **Lan, M**, **Laukert, G**, **Lei, R**, **Li, T**, **Torres-Valdés, S**, **Lin, L**, **Lin, L**, **Liu, H**, **Liu, N**, **Loose, B**, **Ma, X**, **MacKay, R**, **Mallet, M**, **Mallett, RDC**, **Maslowski, W**, **Mertens, C**, **Mohrholz, V**, **Muilwijk, M**, **Nicolaus, M**, **O'Brien, JK**, **Perovich, D**, **Ren, J**, **Rex, M**, **Ribeiro, N**, **Rinke, A**, **Schaffer, J**, **Schuffenhauer, I**, **Schulz, K**, **Shupe, MD**, **Shaw, W**, **Sokolov, V**, **Sommerfeld, A**, **Spreen, G**, **Stanton, T**, **Stephens, M**, **Su, J**, **Sukhikh, N**, **Sundfjord, A**, **Thomisch, K**, **Tippenhauer, S**, **Toole, JM**, **Vredenborg, M**, **Walter, M**, **Wang, H**, **Wang, L**, **Wang, Y**, **Wendisch, M**, **Zhao, J**, **Zhou, M**, **Zhu, J**. 2022.

Overview of the MOSAiC expedition: Physical oceanography. *Elementa: Science of the Anthropocene* **10**(1): 00062. DOI: https://dx.doi.org/10.1525/elementa.2021.00062.

Rampal, P, **Weiss, J**, **Marsan, D.** 2009. Positive trend in the mean speed and deformation rate of Arctic sea ice, 1979–2007. *Journal of Geophysical Research: Oceans* **114**(C5).

Raphael, I, **Clemens-Sewall, D**, **Perovich, D**, **Polashenski, C.** 2024. Snow–ice interface temperatures from the Multidisciplinary drifting Observatory for the Study of Arctic Climate (MOSAiC) expedition in the central Arctic (2019–2020) [dataset]. Arctic Data Center. DOI: https://dx.doi.org/10.18739/A2MP4VQ0X.

Raphael, I, **Clemens-Sewall, D**, **Perovich, D**, **Polashenski, C**, **Itkin, P**, **Regnery, J**, **Nicolaus, M**, **Jaggi, M**, **Smith, M**, **Matero, I**, **Macfarlane, A**, **Hutchings, J**, **Jutila, A**, **Fons, S**, **Oggier, M**, **Wagner, D**, **Demir, O.** 2022. Measurements of sea ice point-mass-balance using hotwire thickness gauges and ablation stakes during the Multidisciplinary drifting Observatory for the Study of Arctic Climate (MOSAiC) Expedition in the Central Arctic (2019–2020) [dataset]. Arctic Data Center. DOI: https://dx.doi.org/10.18739/A2NK36626.

Richter-Menge, JA, **Perovich, DK**, **Elder, BC**, **Claffey, K**, **Rigor, I**, **Ortmeyer, M**. 2006. Ice mass-balance buoys: A tool for measuring and attributing changes in the thickness of the Arctic sea-ice cover. *Annals of Glaciology* **44**: 205–210.

Rinke, A, **Cassano, JJ**, **Cassano, EN**, **Jaiser, R**, **Handorf, D.** 2021. Meteorological conditions during the MOSAiC expedition: Normal or anomalous? *Elementa: Science of the Anthropocene* **9**(1): 00023. DOI: https://dx.doi.org/10.1525/elementa.2021.00023.

Roesel, A, **Itkin, P**, **King, J**, **Divine, D**, **Wang, C**, **Granskog, MA**, **Krumpen, T**, **Gerland, S.** 2018. Thin sea ice, thick snow, and widespread negative freeboard observed during N-ICE2015 north of Svalbard. *Journal of Geophysical Research: Oceans* **123**(2): 1156–1176.

Salganik, E, **Katlein, C**, **Lange, BA**, **Matero, I**, **Lei, R**, **Fong, AA**, **Fons, SW**, **Divine, D**, **Oggier, M**, **Castellani, G**, **Bozzato, D**, **Chamberlain, EJ**, **Hoppe, CJM**, **Müller, O**, **Gardner, J**, **Rinke, A**, **Pereira, PS**, **Ulfsbo, A**, **Marsay, C**, **Webster, MA**, **Maus, S**, **Høyland, KV**, **Granskog, MA.** 2023a. Temporal evolution of under-ice meltwater layers and false bottoms and their impact on summer Arctic sea ice mass balance. *Elementa: Science of the Anthropocene* **11**(1): 00035. DOI: https://dx.doi.org/10.1525/elementa.2022.00035.

Salganik, E, **Lange, BA**, **Katlein, C**, **Matero, I**, **Anhaus, P**, **Muilwijk, M**, **Høyland, KV**, **Granskog, MA.** 2023b. Observations of preferential summer melt of Arctic sea-ice ridge keels from repeated multibeam sonar surveys. *The Cryosphere* **17**(11): 4873–4887. DOI: https://dx.doi.org/10.5194/tc-17-4873-2023.

Schulz, K, **Koenig, Z**, **Muilwijk, M.** 2023. The Eurasian Arctic ocean along the MOSAiC drift (2019–2020): Core hydrographic parameters [dataset]. Arctic Data Center. DOI: https://dx.doi.org/10.18739/A21J9790B.

Shupe, MD, **Rex, M**, **Blomquist, B**, **Persson, POG**, **Schmale, J**, **Uttal, T**, **Althausen, D**, **Angot, H**, **Archer, S**, **Bariteau, L**, **Beck, I**, **Bilberry, J**, **Bucci, S**, **Buck, C**, **Boyer, M**, **Brasseur, Z**, **Brooks, IM**, **Calmer, R**, **Cassano, J**, **Castro, V**, **Chu, D**, **Costa, D**, **Cox, CJ**, **Creamean, J**, **Crewell, S**, **Dahlke, S**, **Damm, E**, **de Boer, G**, **Deckelmann, H**, **Dethloff, K**, **Dütsch, M**, **Ebell, K**, **Ehrlich, A**, **Ellis, J**, **Engelmann, R**, **Fong, AA**, **Frey, MM**, **Gallagher, MR**, **Ganzeveld, L**, **Gradinger, R**, **Graeser, J**, **Greenamyer, V**, **Griesche, H**, **Griffiths, S**, **Hamilton, J**, **Heinemann, G**, **Helmig, D**, **Herber, A**, **Heuzé, C**, **Hofer, J**, **Houchens, T**, **Howard, D**, **Inoue, J**, **Jacobi, H-W**, **Jaiser, R**, **Jokinen, T**, **Jourdan, O**, **Jozef, G**, **King, W**, **Kirchgaessner, A**, **Klingebiel, M**, **Krassovski, M**, **Krumpen, T**, **Lampert, A**, **Landing, W**, **Laurila, T**, **Lawrence, D**, **Lonardi, M**, **Loose, B**, **Lüpkes, C**, **Maahn, M**, **Macke, A**, **Maslowski, W**, **Marsay, C**, **Maturilli, M**, **Mech, M**, **Morris, S**, **Moser, M**, **Nicolaus, M**, **Ortega, P**, **Osborn, J**, **Pätzold, F**, **Perovich, DK**, **Petäjä, T**, **Pilz, C**, **Pirazzini, R**, **Posman, K**, **Powers, H**, **Pratt, KA**, **Preußer, A**, **Quéléver, L**, **Radenz, M**, **Rabe, B**, **Rinke, A**, **Sachs, T**, **Schulz, A**, **Siebert, H**, **Silva, T**, **Solomon, A**, **Sommerfeld, A**, **Spreen, G**, **Stephens, M**, **Stohl, A**, **Svensson, G**, **Uin, J**, **Viegas, J**, **Voigt, C**, **von der Gathen, P**, **Wehner, B**, **Welker, JM**, **Wendisch, M**, **Werner, M**, **Xie, ZQ**, **Yue, F**. 2022. Overview of the MOSAiC expedition: Atmosphere. *Elementa: Science of the Anthropocene* **10**(1): 00060. DOI: https://dx.doi.org/10.1525/elementa.2021.00060.

Skyllingstad, ED, **Paulson, CA.** 2007. A numerical study of melt ponds. *Journal of Geophysical Research: Oceans* **112**(C8).

Sledd, A, **Shupe, M**, **Solomon, A**, **Perovich, DK**, **Lei, R**. 2022. Snow thermal conductivity and conductive flux variability during the MOSAiC winter. Fall Meeting 2022. Washington, DC: AGU.

Smith, MM, **Angot, H**, **Chamberlain, EJ**, **Droste, ES**, **Karam, S**, **Muilwijk, M**, **Webb, AL**, **Archer, SD**, **Beck, I**, **Blomquist, BW**, **Bowman, J**, **Boyer, M**, **Bozzato, D**, **Chierici, M**, **Creamean, J**, **D'Angelo, A**, **Delille, B**, **Fer, I**, **Fong, AA**, **Fransson, A**, **Fuchs, N**, **Gardner, J**, **Granskog, MA**, **Hoppe, CJM**, **Hoppema, M**, **Hoppmann, M**, **Mock, T**, **Muller, S**, **Müller, O**, **Nicolaus, M**, **Nomura, D**, **Petäjä, T**, **Salganik, E**, **Schmale, J**, **Schmidt, K**, **Schulz, K**, **Shupe, MD**, **Stefels, J**, **Thielke, L**, **Tippenhauer, S**, **Ulfsbo, A**, **van Leeuwe, M**, **Webster, M**, **Yoshimura, M**, **Zhan, L**. 2023. Thin and transient meltwater layers and false bottoms in the Arctic sea ice pack—Recent insights on these historically overlooked features. *Elementa: Science of the*

Anthropocene **11**(1): 00025. DOI: https://dx.doi.org/10.1525/elementa.2023.00025.

Smith, MM, **von Albedyll, L**, **Raphael, IA**, **Lange, BA**, **Matero, I**, **Salganik, E**, **Webster, MA**, **Granskog, MA**, **Fong, A**, **Lei, R**, **Light, B.** 2022. Quantifying false bottoms and under-ice meltwater layers beneath Arctic summer sea ice with fine-scale observations. *Elementa: Science of the Anthropocene* **10**(1): 000116. DOI: https://dx.doi.org/10.1525/elementa.2021.000116.

Smith, N. 2019. Mathematical modelling of under-ice melt ponds and their impact on the thermohaline interaction between sea ice and the oceanic mixed layer [Doctoral dissertation]. Berkshire, UK: University of Reading.

Stroeve, J, **Notz, D**. 2018. Changing state of Arctic sea ice across all seasons. *Environmental Research Letters* **13**(10): 103001.

Stroeve, JC, **Markus, T**, **Boisvert, L**, **Miller, J**, **Barrett, A.** 2014. Changes in Arctic melt season and implications for sea ice loss. *Geophysical Research Letters* **41**(4): 1216–1225.

Sturm, M, **Massom, RA**. 2017. Snow in the sea ice system: Friend or foe? in Thomas, DN ed., *Sea ice*. Hoboken, NJ: John Wiley & Sons, Inc.: 65–109.

Sturm, M, **Perovich, DK**, **Holmgren, J**. 2002. Thermal conductivity and heat transfer through the snow on the ice of the Beaufort Sea. *Journal of Geophysical Research: Oceans* **107**(C10): SHE 19-1–SHE 19-17.

Sumata, H, **de Steur, L**, **Divine, DV**, **Granskog, MA**, **Gerland, S.** 2023. Regime shift in Arctic Ocean sea ice thickness. *Nature* **615**(7952): 443–449.

Sumata, H, **de Steur, L**, **Gerland, S**, **Divine, DV**, **Pavlova, O.** 2022. Unprecedented decline of Arctic sea ice outflow in 2018. *Nature Communications* **13**(1): 1747.

Turner, AK, **Hunke, EC.** 2015. Impacts of a mushy-layer thermodynamic approach in global sea-ice simulations using the CICE sea-ice model. *Journal of Geophysical Research: Oceans* **120**(2): 1253–1275. DOI: https://dx.doi.org/10.1002/2014JC010358.

Untersteiner, N. 1961. On the mass and heat budget of Arctic sea ice. *Archiv für Meteorologie, Geophysik und Bioklimatologie, Serie A* **12**: 151–182.

Uttal, T, **Curry, JA**, **McPhee, MG**, **Perovich, DK**, **Moritz, RE**, **Maslanik, JA**, **Guest, PS**, **Stern, HL**, **Moore, JA**, **Turenne, R**, **Heiberg, A**, **Serreze, MC**, **Wylie, DP**, **Persson, OG**, **Paulson, CA**, **Halle, C**, **Morison, JH**, **Wheeler, PA**, **Makshtas, A**, **Welch, H**, **Shupe, MD**, **Intrieri, JM**, **Stamnes, K**, **Lindsey, RW**, **Pinkel, R**, **Pegau, WS**, **Stanton, TP**, **Grenfeld, TC.** 2002. Surface heat budget of the Arctic Ocean. *Bulletin of the American Meteorological Society* **83**(2): 255–276.

von Albedyll, L, **Hendricks, S**, **Grodofzig, R**, **Krumpen, T**, **Arndt, S**, **Belter, HJ**, **Cheng, B**, **Birnbaum, G**, **Hoppmann, M**, **Hutchings, J**, **Itkin, P**, **Lei, R**, **Nicolaus, M**, **Ricker, R**, **Rohde, J**, **Suhrhoff, M**, **Timofeeva, A**, **Watkins, D**, **Webster, M**, **Haas, C.** 2022. Thermodynamic and dynamic contributions to seasonal Arctic sea ice thickness distributions from airborne observations. *Elementa: Science of the Anthropocene* **10**(1): 00074. DOI: https://dx.doi.org/10.1525/elementa.2021.00074.

Wang, C, **Granskog, MA**, **Hudson, SR**, **Gerland, S**, **Pavlov, AK**, **Perovich, DK**, **Nicolaus, M.** 2016. Atmospheric conditions in the central Arctic Ocean through the melt seasons of 2012 and 2013: Impact on surface conditions and solar energy deposition into the ice-ocean system. *Journal of Geophysical Research: Atmospheres* **121**(3): 1043–1058.

Webster, MA, **Holland, M**, **Wright, NC**, **Hendricks, S**, **Hutter, N**, **Itkin, P**, **Light, B**, **Linhardt, F**, **Perovich, DK**, **Raphael, IA**, **Smith, MM**, **von Albedyll, L**, **Zhang, J.** 2022. Spatiotemporal evolution of melt ponds on Arctic sea ice: MOSAiC observations and model results. *Elementa: Science of the Anthropocene* **10**(1): 000072. DOI: https://dx.doi.org/10.1525/elementa.2021.000072.

Zhang, J. 2021. Recent slowdown in the decline of Arctic sea ice volume under increasingly warm atmospheric and oceanic conditions. *Geophysical Research Letters* **48**(18): e2021GL094780.

How to cite this article: Raphael, IA, Perovich, DK, Polashenski, CM, Clemens-Sewall, D, Itkin, P, Lei, R, Nicolaus, M, Regnery, J, Smith, MM, Webster, M, Jaggi, M. 2024. Sea ice mass balance during the MOSAiC drift experiment: Results from manual ice and snow thickness gauges. *Elementa: Science of the Anthropocene* 12(1). DOI: https://doi.org/10.1525/elementa.2023.00040

Domain Editor-in-Chief: Jody W. Deming, University of Washington, Seattle, WA, USA

Associate Editor: Stephen F. Ackley, Department of Geological Sciences, University of Texas at San Antonio, TX, USA

Knowledge Domain: Ocean Science

Part of an Elementa Special Feature: The Multidisciplinary Drifting Observatory for the Study of Arctic Climate (MOSAiC)

Published: July 09, 2024 **Accepted:** May 01, 2024 **Submitted:** March 13, 2023

ELEMENTA Science of the Anthropocene

Elem Sci Anth is a peer-reviewed open access journal published by University of California Press.

OPEN ACCESS